Old Dominion University

ODU Digital Commons

Mechanical & Aerospace Engineering Theses & Dissertations

Mechanical & Aerospace Engineering

Fall 1990

Integrated Control of Thermally Distorted Large Space Antennas

Robert H. Tolson
Old Dominion University

Follow this and additional works at: https://digitalcommons.odu.edu/mae_etds

 Part of the Applied Mechanics Commons, Electrical and Electronics Commons, Remote Sensing Commons, and the Structures and Materials Commons

Recommended Citation

Tolson, Robert H.. "Integrated Control of Thermally Distorted Large Space Antennas" (1990). Doctor of Philosophy (PhD), Dissertation, Mechanical & Aerospace Engineering, Old Dominion University, DOI: 10.25777/ykb9-dk95
https://digitalcommons.odu.edu/mae_etds/277

This Dissertation is brought to you for free and open access by the Mechanical & Aerospace Engineering at ODU Digital Commons. It has been accepted for inclusion in Mechanical & Aerospace Engineering Theses & Dissertations by an authorized administrator of ODU Digital Commons. For more information, please contact digitalcommons@odu.edu.

INTEGRATED CONTROL OF THERMALLY DISTORTED LARGE SPACE ANTENNAS

by

Robert H.Tolson
B.S. June 1958, Virginia Polytechnic Institute
M.S. June 1963, Virginia Polytechnic Institute

A Dissertation Submitted to the Faculty of Old Dominion University in Partial Fulfillment of the Requirements for the Degree of

DOCTOR OF PHILOSOPHY

ENGINEERING MECHANICS

OLD DOMINION UNIVERSITY
October, 1990

Approved by:

Dr. Jen-Kuang Huang (Director)

Dr. Robert L. Ash

Dr. Marion C. Bailey

Dr. L. Bernard Garrett

Dr. Chuh Mei

Reproduced with permission of the copyright owner. Further reproduction prohibited without permission.

ABSTRACT

INTEGRATED CONTROL OF THERMALLY DISTORTED LARGE SPACE ANTENNAS

Robert H. Tolson
Old Dominion University, 1990
Director: Dr. Jen-Kuang Huang

Studies on controlling the thermal distortion of large space antennae have generally investigated a single orbital position and have optimized actuator locations based on minimizing the RMS surface deviation from the original parabolic shape. One study showed the benefits of directly using far zone electric field characteristics as the performance measure; but, this approach resulted in a nonlinear programming problem. The objective of the current study is to develop an approach to designing a control system that (1) recognizes the time dependence of the distortion and (2) controls variables that are directly related to far field performance in a quadratic cost sense. The first objective, to explicitly include the time dependence, is accomplished using a principal component analysis to expand an "aperture phase function" into components that are orthogonal in space and time. The aperture phase function is readily calculable from surface distortion and accommodates tapered feeds and arbitrary polarizations. Actuator strokes are shown to be linear combinations of the time dependent components. The spatial components provide a natural space in which to determine the optimal actuator locations and as basis vectors for extrapolating sensor measurements to the entire antenna surface. The approach for the second objective is to expand the far zone electric field in a Zernike-Bessel series. For surface distortions of less than a quarter wavelength, it is shown that the coefficients of this series provide a reliable measure of far field performance. Simulations are performed for a geosynchronous radiometer to determine the robustness of both the open and closed loop systems to variations in solar geometry, structure materials and thermal properties.

Reproduced with permission of the copyright owner. Further reproduction prohibited without permission.

ACKNOWLEDGEMENTS

I would like to take this opportunity to express my gratitude to my advisor, Dr. Jen-Kuang Huang, for his help in planning and executing the academic and research programs and his guidance through the administrative maze.

Thanks also to Dr. Acosta for supplying the RF performance program and to Kathy Young for her never ending patience and help with the documentation process.

Finally, thanks to Carol, to whom this effort is dedicated, for understanding my occasional trips to never-never land during the last few months.

Reproduced with permission of the copyright owner. Further reproduction prohibited without permission.

TABLE OF CONTENTS

Reproduced with permission of the copyright owner. Further reproduction prohibited without permission.

LIST OF TABLES

Reproduced with permission of the copyright owner. Further reproduction prohibited without permission.

LIST OF FIGURES

Reproduced with permission of the copyright owner. Further reproduction prohibited without permission.

LIST OF FIGURES, Continued

Reproduced with permission of the copyright owner. Further reproduction prohibited without permission.

LIST OF SYMBOLS

$\vec{A}_{nm}$	amplitude of Zernike polynomial expansion for $\vec{U}$.
$\vec{B}_{nm}$	amplitude of Zernike polynomial expansion for $\vec{V}$.
$\vec{C}_{nm}$	amplitude of Zernike polynomial expansion for $\vec{W}$.
CTE	coefficient of thermal expansion, K^{-1}.
$\boldsymbol{E}$	matrix of principal component eigenvectors.
$\vec{E}_i$	electric field incident on the antenna surface, $^{volts}/_{m}$.
F	focal length of antenna, m.
$\boldsymbol{F}_{e\alpha}$	principal component projection of $\boldsymbol{G}_\alpha$.
G	feed gain function.
$\boldsymbol{G}$	far field distortion matrix.
$\boldsymbol{G}_e$	principal component projection of $\boldsymbol{G}$.
$\boldsymbol{G}_\alpha$	far field distortion matrix due to unit stroke in α-th actuator.
$\boldsymbol{H}$	Grammian matrix.
J_1	Zernike-Bessel cost.
J_2	Zernike-Bessel average cost over an orbit.
$\vec{J}_S$	antenna surface currents, $^{amps}/_{meter}$.
L	number of principal components used to calculate ε_α.
M	number of actuators.
N	number of points used to discretize the far field integral.
N_{nm}	Zernike polynomial normalization factor.
P	satellite period (sec) or number of PC's estimated from sensor data.
$\boldsymbol{P}$	least square projector.
PC	principal component.
P_t	total power radiated by the feed, watts.

Reproduced with permission of the copyright owner. Further reproduction prohibited without permission.

LIST OF SYMBOLS, Continued

R	distance from focus to far field point, m.
RF	radio frequency.
RMS	root mean square.
R_{nm}	Zernike radial polynomial.
S	number of sensors.
T	temperature of antenna rod, K.
$\vec{U}$	integrand of far field integral due to parabolic shape.
$\vec{V}$	in phase integrand of far field integral due to distorted shape.
$\vec{W}$	quadrature integrand of far field integral due to distorted shape.
a	antenna radius, m.
c	speed of light, $^{m}/_{s}$ or specific heat, $^{J}/_{kgK}$.
d	outer diameter of antenna rods, m.
$\vec{e_1},..., \vec{e_N}$	principal component eigenvectors.
$\vec{e_i}$	unit vector in direction of incident electric field.
$\vec{e_n}$	unit vector normal to antenna surface.
$\vec{e_R}$	unit vector from focus to far field point.
$\vec{e_\rho}$	unit vector from focus to antenna surface.
g_i	amplitude of i-th principal component.
k	wave number, $^{2\pi}/_{\lambda}$, m^{-1}.
l	length of antenna rod, m.
m	mass of antenna rod, kg.
q_e	radiation emitted from the earth, $^{w}/_{m^2}$.
q_s	radiation emitted from the sun, $^{w}/_{m^2}$.
r	radial position of antenna surface points, m.
s_α	stroke of α-th actuator, m.
s	vector of actuator strokes, m.

Reproduced with permission of the copyright owner. Further reproduction prohibited without permission.

LIST OF SYMBOLS, Continued

$\vec{u}$	$\vec{e_n}\times(\vec{e_\rho}\times\vec{e_i})$.
Θ	polar angular position of far field point.
Φ	azimuthal angular position of far field point.
α_e	absorbitivity for earth emitted radiation.
α_s	absorbitivity for solar emitted radiation.
$\vec{\alpha}_{nm}$	phase of Zernike polynomial expansion for $\vec{U}$.
$\vec{\beta}_{nm}$	phase of Zernike polynomial expansion for $\vec{V}$.
$\vec{\gamma}_{nm}$	phase of Zernike polynomial expansion for $\vec{W}$.
γ	$ka\ \sin\Theta$, argument of Bessel series expansion.
δ_i^j	Kronecker delta.
ε	free space permittivity or rod emissivity.
ε_α	rod effectiveness ratio.
$\varepsilon_{\alpha\beta}$	rod correlation ratio.
λ	electromagnetic wavelength, m.
μ	free space permeability.
η	intrinsic impedance of free space.
φ	azimuthal angular position of antenna surface points.
ρ	distance from focus to point on antenna surface, m.
σ	Stefan-Boltzman constant, $^{w}/_{m^2}$.
σ_i^2	principal component eigenvalues.
τ	non-dimensional radius ot the antenna.
θ	polar angular position of antenna surface points.
ω	electromagnetic angular frequency, s^{-1}.

Reproduced with permission of the copyright owner. Further reproduction prohibited without permission.

Chapter 1 - Introduction

Large space antennas have been proposed for numerous applications over the last 20 years. Civil applications generally have included communications, astrophysics, and earth observation. In almost every application there is a demand for a "larger" dish to either increase resolution and/or gain. In the earth observation area, a recent report[1] has recommended a "Mission to Planet Earth" as one of the grand challenges. This "Mission" involves extensive remote observations of the Earth from orbiting platforms. To make the proposed observations will require sensors with wavelengths that range from shorter than visible light to as long as millimeter radio waves. The large space antenna applications are of course at these longer wavelengths. Radio frequencies between 1 and 37 gigahertz (GHz) are particularly useful for measuring water related characteristics of the earth. The 1979 World Administrative Radio Conference[2] has allocated various microwave frequencies for passive remote sensing. Specifically, the band at 1.4 GHz is useful[3] for measuring soil moisture and ocean salinity, bands between 2.6 and 7 GHz are for sea surface temperature, and bands between 6.4 and 15.4 GHz can be used for wind, rain and ice measurements. Frequencies between 11 and 37 GHz are useful for atmospheric water vapor, rain, ocean ice, snow and sea surface state. To achieve 1 to 10 km spatial resolution from Sun synchronous altitudes around 1000 km requires antenna diameters of about 100 meters[3]. To maintain high beam efficiency and reduce side lobe levels, antenna surface accuracy must be maintained between 1/20 and 1/50 of a wavelength. For a 30 GHz signal these correspond to 0.5 and 0.2 mm respectively.

Reproduced with permission of the copyright owner. Further reproduction prohibited without permission.

There are a number of reasons that the surface of an antenna could deviate from the "perfect" parabola. First there are manufacturing and fabrication tolerances. Unlike earth antennas which are designed for the 1-g environment, space antennas most probably could not support their own weight and so cannot be assembled or deployed before launch. Errors in the geometric or physical characteristics must be accommodated in the design process or corrected after assembly in orbit. Hedgepeth[4] shows that the tetrahedral truss is the best structure from the standpoint of minimizing surface shape deviations due to length errors in structural members.

The second source of errors for large space antenna is due to the space environment. These include structural vibration, radiation and thermal expansion. There is an extensive research activity currently underway to develop methods to control the vibration of large space structures. The control of thermal distortions for large space structures has not been given as much attention. This is partly due to the assumption that structural components can be fabricated with graphite epoxy to yield nearly zero coefficient of thermal expansion (CTE). This has been demonstrated over a limited range of temperatures. However, Sharp[5] shows that the CTE can be a strong function of temperature and can vary by more than 10E-6 or a factor of two over the range of temperatures expected for orbiting structural members. For a 100 meter antenna this could produce surface distortions of more than 1 mm which would be unacceptable. Additional concerns include the effect of outgassing, space radiation and thermal cycling on the properties of composite members, which can have significant effects[6,7] depending on layup and coatings.

Controlling thermal distortions of optical telescopes has received much attention[8] in recent years under the general research area of active optics. There are some major differences between an orbiting radiometer and an Earth based telescope. First, radiometers have tapered feeds to improve beam efficiency at the expense of antenna efficiency while

Reproduced with permission of the copyright owner. Further reproduction prohibited without permission.

telescopes generally emphasize antenna efficiency and are satisfied with diffraction limited images. The thermal environment for ground based telescopes has a small temperature range, but the heat balance is very difficult to predict because it is due to convection, conduction and radiation in a very complicated geometric enviroment. Orbiting radiometers on the other hand have much larger temperature extremes that are dominated by radiation in a somewhat simpler geometric environment. Attempts to actively control the thermal distortions of terrestrial telescopes have met with some success and this naturally raises the question of controlling thermal distortions of orbiting radiometers.

Antenna surface shape control methods have been developed[9] for single orbital heating conditions (i.e. a static shape control method) based on minimizing the RMS surface deviation over the antenna surface. Optimal actuator locations have also been determined[10] for the same case. No studies address the temporal variation of the field and the subsequent effect on the optimal locations. In addition, radiometer feeds are generally highly tapered. Consequently, since surface errors in highly illuminated areas of the antenna will contribute more to far field distortion than the same error in a lower illuminated area, surface RMS may not be the most appropriate objective function. The effect of random manufacturing errors on the actual far field pattern has been studied[11] using a nonlinear programming approach. This study demonstrates the merits of including far field characteristics in the objective function. However, optimal actuator locations in this study were based on RMS surface deviations and of course no consideration of the temporal variation was included.

The purpose of the current study is to develop a method for actively controlling the RF performance of a radiometer to ameliorate the effect of thermal distortion due to the temperature variations in orbit. Specific objectives include designing a control system that (1) recognizes the time dependence of the distortion and (2) controls variables that

Reproduced with permission of the copyright owner. Further reproduction prohibited without permission.

are directly related to far field performance in a quadratic cost sense. Based on the recognition that over a few orbits the distortion of the antenna can be considered a periodic function, the first objective is accomplished using a principal component analysis to expand an "aperture phase function" into components that are orthogonal in space and time. The aperture phase function is readily calculable from surface distortion and accommodates tapered feeds and arbitrary polarizations. Actuator strokes are shown to be linear combinations of the time dependent components. The spatial components provide a natural space in which to determine the optimal actuator locations and as basis vectors for extrapolating sensor measurements to the entire antenna surface. The approach for the second objective is to expand the far zone electric field in a Zernike-Bessel series. For surface distortions of less than a quarter wavelength, it is shown that the coefficients of this series provide an excellent measure of far field performance. These coefficients are related to the principal component eigenvalues and "significant" principal components are selected on the basis of the root mean square contribution to deviations of the electric field from the nominal field. Simulations are performed for a geosynchronous radiometer to determine the robustness of both the open and closed loop systems to variations in solar geometry and structure material and thermal properties.

Reproduced with permission of the copyright owner. Further reproduction prohibited without permission.

Chapter 2 - Theoretical Developments

In this chapter the theoretical basis will be developed. These developments will include a new Zernike-Bessel expansion of the far zone electric field, developing control system objective or cost functions in terms of this expansion, decomposing the aperture field using a principal component analysis and relating the eigenvalues to the far field, developing a method for optimally locating actuators to correct the errors, and finally, using the principal component eigenvectors to extrapolate sensor measurements to the entire antenna surface.

2.1-Far Field Calculations for Small Deviations from a Parabolic Surface

The objective of this section is to develop a series expansion of the far field for a slightly distorted parabolic antenna. In subsequent sections this expansion will be used to develop control system cost functions that can be easily calculated from the surface distortion without resorting to traditional RF performance calculations, which require extensive computations and are not very amenable to either the design environment or to real time applications. To accomplish this objective, an approximate method for calculating the far field of a radiometer whose parabolic surface has been distorted by less than a quarter of a wave length is developed. Even though this is a receiving antenna, it is traditional to work in terms of a transmitting antenna when developing far field patterns. To calculate the far zone electric field the physical optics approach described in Collin and Zucker[12] will be utilized. In this section, numbers in brackets refer to equations in Collin and Zucker. The coordinate system is shown in figure 2.1-1, where the capital letters

Reproduced with permission of the copyright owner. Further reproduction prohibited without permission.

(R, Θ, Φ) refer to the far field point, the small letters (ρ, θ, φ) refer to a point on the antenna and $r = \rho \sin\theta$ is reserved for the cylindrical coordinate system radius.

The electric field incident on the antenna {17.11} from the feed is

$$\vec{E_i}(\rho, \theta, \varphi) = \left\{ \sqrt{\mu/\varepsilon}\, \frac{P_t}{2\pi}\, G(\theta, \varphi) \right\}^{1/2} \frac{e^{-jk\rho}}{\rho} \vec{e_i} \ \text{volts/meter} \tag{2.1-1}$$

where $\vec{e_i}(\theta, \varphi)$ defines the direction of the incident electric field, which for a y polarized feed would be

$$\vec{e_i} = \frac{\vec{e_\rho} \times (\vec{e_y} \times \vec{e_\rho})}{|\vec{e_\rho} \times \vec{e_y}|}, \tag{2.1-2}$$

and $\vec{e_\rho} = (\cos\varphi \sin\theta, \sin\varphi \sin\theta, \cos\theta)$, P_t is the total power radiated by the feed in watts, G is the feed gain function or the fractional energy radiated in direction (θ, φ), k is the wave number $k = 2\pi/\lambda = \omega/c$ and μ and ε are the free space permeability and permittivity with values $\varepsilon = \frac{10^7}{4\pi c^2}$ farads/m and $\mu = 4\pi \times 10^{-7}$ henrys/m.

Such an incident electric field induces surface currents {17.10} of

$$\vec{J_s} = \frac{2}{\eta}[\, \vec{e_n} \times (\vec{e_\rho} \times \vec{E_i})\,] \ \text{amps/meter}.$$

where $\eta = \sqrt{\mu/\varepsilon} \approx 120\pi$ ohms is the intrinsic impedence and $\vec{e_n}$ is the unit vector normal to the reflector surface. These surface currents produce a far zone electric field given by an integral over the surface of the antenna {3.47}

$$\vec{E}(\Theta, \Phi) = -\frac{j\omega\mu e^{-jkR}}{4\pi R} \iint_S [\, \vec{J_s} - (\vec{J_s} \cdot \vec{e_R})\, \vec{e_R}\,]\, e^{jk\rho(\vec{e_\rho} \cdot \vec{e_R})} dS, \tag{2.1-3}$$

Reproduced with permission of the copyright owner. Further reproduction prohibited without permission.

where $dS = \frac{\rho^2 \sin\theta \, d\theta \, d\varphi}{\left|\vec{e\rho} \cdot \vec{en}\right|}$ and $\vec{eR} = (\cos\Phi \sin\Theta, \sin\Phi \sin\Theta, \cos\Theta)$. For the purposes here, only the radiation pattern near the central lobe is of interest and for the narrow beam antennas that would be used for radiometers it is common to set $\cos\Theta = -1$ and use the approximation $\vec{eR} = (\cos\Phi \sin\Theta, \sin\Phi \sin\Theta, -1)$ in the integral.

The far field has no $\vec{eR}$ component and the other two components are given by {17.19}

$$E_\Theta = -\frac{j\omega\mu e^{-jkR}}{4\pi R} \iint_S \vec{e\Theta} \cdot \vec{J_S} e^{jk\rho(\vec{e\rho} \cdot \vec{eR})} dS \quad \text{and}$$

$$E_\Phi = -\frac{j\omega\mu e^{-jkR}}{4\pi R} \iint_S \vec{e\Phi} \cdot \vec{J_S} e^{jk\rho(\vec{e\rho} \cdot \vec{eR})} dS, \tag{2.1-4}$$

where $\vec{e\Theta} = (\cos\Phi\cos\Theta, \sin\Phi\cos\Theta, -\sin\Theta)$ and $\vec{e\Phi} = (-\sin\Phi, \cos\Phi, 0)$. The z-component of E_Φ is zero and the z- component of E_Θ is proportional to $\sin\Theta$, which may be neglected near the central beam. Thus the integral of interest

$$\vec{E} = -\frac{j\omega\mu e^{-jkR}}{4\pi R} \iint_S \vec{J_S} e^{jk\rho(\vec{e\rho} \cdot \vec{eR})} dS$$

may be approximated as a two-vector. However, for completeness the three-vector nature will be maintained during the theoretical development; but, the two vector approach will be used for the validation studies for reasons to be discussed later.

Substituting for $\vec{J_S}$ and $\vec{E_i}$ and collecting terms outside the integral into

$$C_2 = -\frac{j\omega\mu \, e^{-jkR}}{2\pi R\eta} \left\{\sqrt{\mu/\varepsilon}\frac{P_t}{2\pi}\right\}^{1/2} \ volts/meter^2$$

Reproduced with permission of the copyright owner. Further reproduction prohibited without permission.

gives

$$\vec{E} = C_2 \iint_S \vec{u}\sqrt{G}\,\frac{e^{-jk\rho(1-\vec{e_\rho}\cdot\vec{e_R})}}{\rho}\,dS. \tag{2.1-5}$$

where $\vec{u} = \vec{e_n}\times(\vec{e_\rho}\times\vec{e_i})$.

The next step is to evaluate the integral 2.1-5 for a reflector with a surface that is distorted from the desired parabolic shape. To evaluate the integral only the effects of distortion on the phase of the reflected rays will be considered, that is, the effects of distortion on ray direction and angular spreading are neglected. This approximation will only be used in developing an objective function for control system design. Far field patterns, to be presented later, are based on a complete physical optics simulation[13] which include changes in the slope of the surface.

For a parabolic reflector

$$\rho = \frac{2F}{1+\cos\theta}, \tag{2.1-6}$$

where F is the focal length. As seen from figure 2.1-2, the distance a ray travels from the focus to the reflector and back to the aperture plane through the focal point is $\rho+\rho\cos\theta$ or 2F. For a distorted surface the distance will no longer be 2F, but will be modeled as

$$\Psi(\theta,\varphi) = \rho(\theta,\varphi)(1+\cos\theta) - 2F. \tag{2.1-7}$$

Ψ is then similiar to the wave aberration function discussed in Born.[14] If the distorted surface is modeled as displacements in the z direction δz, then the relation between Ψ and δz can be obtained by refering to figure 2.1-2. The displacements are assumed to be small compared to the focal length. The path length for the undistorted surface is FA +

Reproduced with permission of the copyright owner. Further reproduction prohibited without permission.

AP and for the distorted surface is FB + BQ. The difference is Ψ = AB + BD. Now CB is the z displacement δz. Since the rays satisfy Snell's law at the surface, ABC is an isosceles triangle and so AB = BC = δz. Since BD = BC cosθ,

$$\Psi \approx (1+\cos\theta)\delta z, \tag{2.1-8}$$

which is linear in the displacement and depends on the location on the antenna. Using the relation between ρ and Ψ in the phase part of the integral along with the approximation $\vec{eR} = (\cos\Phi \sin\Theta, \sin\Phi \sin\Theta, -1)$ from above gives in the exponent

$$\rho(1 - \vec{e_\rho}\cdot\vec{eR}) = 2F + \Psi - \rho \sin\theta \sin\Theta \cos(\Phi - \varphi).$$

Thus

$$e^{-jk\rho(1 - \vec{e_\rho}\cdot\vec{eR})} = e^{-2jkF}\, e^{-jk\Psi}\, e^{jk\rho\sin\theta \sin\Theta \cos(\Phi - \varphi)}.$$

The first term is a constant and combined into C_2 to give $C_1 = e^{-2jkF}\, C_2$. The second term can be written as

$$e^{-jk\Psi} = 1 - 2\sin^2\frac{k\Psi}{2} - j\sin k\Psi.$$

So that

$$\vec{E} = C_1 \iint_S \vec{u}\sqrt{G(\theta, \varphi)}\,(1 - 2\sin^2\frac{k\Psi}{2} - j\sin k\Psi)\,\frac{e^{jk\rho\sin\theta \sin\Theta \cos(\Phi - \varphi)}}{\rho}\,dS.$$

It is now convenient to change variables from θ to r using $r = \rho \sin\theta$. Evaluating differentials on a parabolic surface { 17.2 & 17.4 } leads to $dr = \rho\, d\theta$, and the integral becomes

Reproduced with permission of the copyright owner. Further reproduction prohibited without permission.

$$\vec{E} = C_1 \int_0^{2\pi} \int_0^{a} \vec{u}\sqrt{G}\,(1-2\sin^2\frac{k\Psi}{2} - j\sin k\Psi)\,\frac{e^{jkr\,\sin\Theta\cos(\Phi-\varphi)}}{\rho\cos\theta/2}\,r\,dr\,d\varphi,$$

where the antenna radius is 'a' and $\left|\vec{e_\rho}\cdot\vec{e_n}\right| = \cos\theta/2$ has been used. In the exponential, terms of order $\Psi\sin\Theta$, which are of second order near the central beam, were neglected. The denominator is also evaluated on the parabola so that $\rho\cos\theta/2 = \frac{F}{\cos\theta/2}$. Let $\tau = r/a$ be the non-dimensional radius and combine the focal length F and a^2 with C_1 to give $C = C_1\, a^2/F$ to yield the final expression for the far zone electric field,

$$\vec{E} = C \int_0^{2\pi} \int_0^{1} \vec{u}\sqrt{G}\,(1-2\sin^2\frac{k\Psi}{2} - j\sin k\Psi)\,\cos\theta/2\, e^{jka\tau\,\sin\Theta\cos(\Phi-\varphi)}\,\tau\,d\tau\,d\varphi, \qquad (2.1\text{-}9)$$

where $C = -\frac{j\omega\mu a^2\, e^{-jk(R+2F)}}{2\pi RF\eta}\left\{\sqrt{\mu/\varepsilon}\,\frac{P_t}{2\pi}\right\}^{1/2}$ *volts/meter*

Thus the far zone field can be written as the sum of a field from the undistorted reflector and a field determined by the distortion.

The integral in equation 2.1-9 will now be reduced to an infinite series by using Zernike polynomial expansions (see appendix A). The Zernike polynomials are complete with respect to the ring of polynomials in x and y on the unit circle and if $\vec{u}, G$, and Ψ admit to Taylor series expansions then vectors $\vec{A}_{nm}$, $\vec{B}_{nm}$, $\vec{C}_{nm}$, $\vec{\alpha}_{nm}$, $\vec{\beta}_{nm}$, and $\vec{\gamma}_{nm}$ exist such that

$$\vec{U}(\theta, \varphi) \equiv \vec{u}\sqrt{G}\,\cos\theta/2 = \sum_{n,m} \vec{A}_{nm}\, R_{nm}(\tau)\,\cos m(\varphi - \vec{\alpha}_{nm}) \qquad (2.1\text{-}10)$$

$$\vec{V}(\theta, \varphi) \equiv 2\vec{U}(\theta, \varphi)\sin^2\frac{k\Psi}{2} = \sum_{n,m} \vec{B}_{nm}\, R_{nm}(\tau)\,\cos m(\varphi - \vec{\beta}_{nm}). \qquad (2.1\text{-}11)$$

Reproduced with permission of the copyright owner. Further reproduction prohibited without permission.

and

$$\vec{W}(\theta, \varphi) \equiv \vec{U}(\theta, \varphi)\sin k\Psi = \sum_{n,m} \vec{C}_{nm} R_{nm}(\tau) \cos m(\varphi - \vec{\gamma}_{nm}), \tag{2.1-12}$$

where the relation $\theta = 2 \tan^{-1}\left(\frac{\tau a}{2F}\right)$ is used to eliminate θ in favor of τ. The sums are for n from 0 to ∞ and for m from 0 to n with n-m even. The notation for the phase is non-conventional; but, the meaning is that if the x component of $\vec{U}$ is being calculated, then the x component of $\vec{A}_{nm}$ and the x component of $\vec{\alpha}_{nm}$ should be used in the sum.

Introduce these two expansions and the well used Bessel expansion

$$e^{jka\tau \sin\Theta \cos(\Phi - \varphi)} = J_0(ka\tau \sin\Theta) + 2 \sum_{p=1}^{\infty} j^p J_p(ka\tau \sin\Theta) \cos p(\Phi - \varphi)$$

into the integral. Then integrate with respect to φ term by term using the usual Fourier orthogonality conditions and in particular

$\int_0^{2\pi} \cos n(\varphi - \alpha) \cos m(\varphi - \beta)\, d\varphi = \pi\,(1 + \delta_m^0)\cos n(\alpha - \beta)\delta_n^m$, where δ_n^m is the Kronecker delta,

to get

$$\vec{E} = 2\pi C \int_0^1 \sum_{n,m} j^m (1 + \delta_m^0) \times$$

$$\left\{\vec{A}_{nm} \cos m(\Phi - \vec{\alpha}_{nm}) - \vec{B}_{nm} \cos m(\Phi - \vec{\beta}_{nm}) - j\vec{C}_{nm} \cos m(\Phi - \vec{\gamma}_{nm})\right\} R_{nm}(\tau) J_m(\gamma\tau)\, \tau d\tau,$$

where $\gamma = ka\sin\Theta$. The main advantage of using Zernike polynomials is the relation (Born, 1980, pg. 772)

Reproduced with permission of the copyright owner. Further reproduction prohibited without permission.

$$\int_0^1 R_{nm}(\tau)\, J_m(\gamma\tau)\tau\, d\tau = (-1)^{\frac{n-m}{2}}\, \frac{J_{n+1}(\gamma)}{\gamma}$$

which reduces the last integral to evaluating the infinite series

$$\vec{E} = 2\pi C \sum_n \frac{J_{n+1}(\gamma)}{\gamma} \sum_m j^m (1+\delta_m^o)(-1)^{\frac{n-m}{2}} \times$$

$$\left\{\vec{A}_{nm}\cos m(\Phi-\vec{\alpha}_{nm}) - \vec{B}_{nm}\cos m(\Phi-\vec{\beta}_{nm}) - j\vec{C}_{nm}\cos m(\Phi-\vec{\gamma}_{nm})\right\}. \qquad (2.1\text{-}13)$$

Thus the far zone electric field, $E_\Theta = \vec{e}_\Theta \cdot \vec{E}$ and $E_\Phi = \vec{e}_\Phi \cdot \vec{E}$, is a sum of Bessel functions that depend only on Θ with amplitude and phase that depend on Φ, $G(\theta,\varphi)$, the feed polarization through $\vec{u}(\theta,\varphi)$ and the surface distortion through $\Psi(\theta, \varphi)$. The coefficients $\vec{A}_{nm}$ determine the field of the undistorted reflector and the coefficients $\vec{B}_{nm}$ and $\vec{C}_{nm}$ determine the field due to the distortions of the reflector. The $\vec{B}_{nm}$ terms are in phase with the $\vec{A}_{nm}$ while the $\vec{C}_{nm}$ are quadrature terms being $\pi/2$ out of phase. Both of these effects contribute to distorting the far zone field; and, in particular, when $\Theta = 0$ only the $n = 0$ term will contribute so that

$$\vec{E}(0, 0) = \pi C \left\{\vec{A}_{00} - \vec{B}_{00} - j\vec{C}_{00}\right\}. \qquad (2.1\text{-}14)$$

It should be noted that $\vec{C}_{00}$ is a generalized "piston" term representing the average phase shift across the aperture weighted by the polarization and the feed gain. The $\vec{B}_{00}$ is a generalized average square phase error and can be interpreted as a generalization of the Ruze criteria.[15] Explicit expressions for $\vec{A}_{nm}$, $\vec{B}_{nm}$ and $\vec{C}_{nm}$ and the corresponding phases can be obtained using expressions from appendix A; namely,

$$\vec{A}_{nm}\, e^{j\vec{\alpha}_{nm}} = \frac{2}{\pi N_{nm}} \int_0^{2\pi} \int_0^1 \vec{U}(\tau, \varphi)\, R_{nm}(\tau)\, e^{jm\varphi}\, \tau\, d\tau\, d\varphi, \qquad (2.1\text{-}15)$$

Reproduced with permission of the copyright owner. Further reproduction prohibited without permission.

$$\vec{B}_{nm}\, e^{j\vec{\beta}_{nm}} = \frac{2}{\pi N_{nm}} \int_0^{2\pi} \int_0^1 \vec{W}(\tau, \varphi)\, R_{nm}(\tau)\, e^{jm\varphi}\, \tau\, d\tau\, d\varphi, \tag{2.1-16}$$

$$\vec{C}_{nm}\, e^{j\vec{\gamma}_{nm}} = \frac{2}{\pi N_{nm}} \int_0^{2\pi} \int_0^1 \vec{W}(\tau, \varphi)\, R_{nm}(\tau)\, e^{jm\varphi}\, \tau\, d\tau\, d\varphi, \tag{2.1-17}$$

where $N_{nm} = \frac{1+\delta_m^0}{n+1}$ is the normalization factor so that the integral of the squared Zernike polynomials over the unit circle are unity (see appendix A).

Recall that $\vec{W} = \vec{u}\sqrt{G}\, \sin k\Psi \cos^{\theta}/_2$, where G is the feed gain function and $\vec{u}$ is a vector of no more than unit length and is determined by the polarization of the feed. For highly tapered feeds the term $\sqrt{G}\cos^{\theta}/_2$ will primarily determine the relative importance of phase errors in the aperture plane. But $\vec{u}$ will also contribute to the relative importance. For example, it can be shown {17.17 & 17.18} that for a y-polarized feed

$$\vec{u} \approx \frac{-\cos^{\theta}/_2 \{\sin\varphi \cos\varphi(1-\cos\theta)\vec{e_x} - (\sin^2\varphi \cos\theta + \cos^2\varphi)\vec{e_y}\} - \sin\varphi \cos\theta \sin^{\theta}/_2\, \vec{e_z}}{\sqrt{1 - \sin^2\varphi \sin^2\theta}} \tag{2.1-18}$$

which is a slowly varying function of θ and φ. If the antenna has a large ratio of F/a then $\cos\theta \approx 1$ and $\vec{u} \approx \vec{e_y}$ is a constant. Feeds can be designed [16] so that the far field has little or no cross polarization, i.e. $\vec{u}$ will have a constant direction. If both $\vec{u}$ and G are constant then $\vec{\gamma}_{nm} = 0$ for all n and m and the expressions reduce to the classical uniform circular aperture case with the C_{nm} representing the classical aberrations. For example, C_{40} is spherical aberration and C_{22} is astigmatism.

From (2.1-18) it is seen that the y-component of $\vec{u}$ is unity to second order in θ and the x-component is zero to second order. The z-component is only zero to first order in θ. To calculate the far field, however, the z-component gets multiplied (2.1-4) by $\sin\Theta$, which

Reproduced with permission of the copyright owner. Further reproduction prohibited without permission.

is small in the area of interest for narrow beam radiometers. Thus, while the z- component is generally larger than the x-component in $\vec{u}$, it's contribution to the far field is actually smaller. This discussion will be used later to justify ignoring the z-component in the calculation of $\vec{C}_{nm}$.

Reproduced with permission of the copyright owner. Further reproduction prohibited without permission.

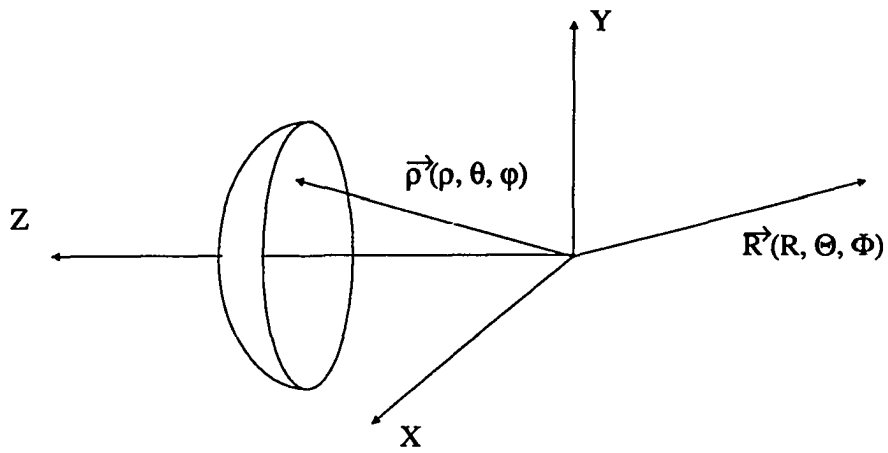

Figure 2.1-1. Coordinate system.

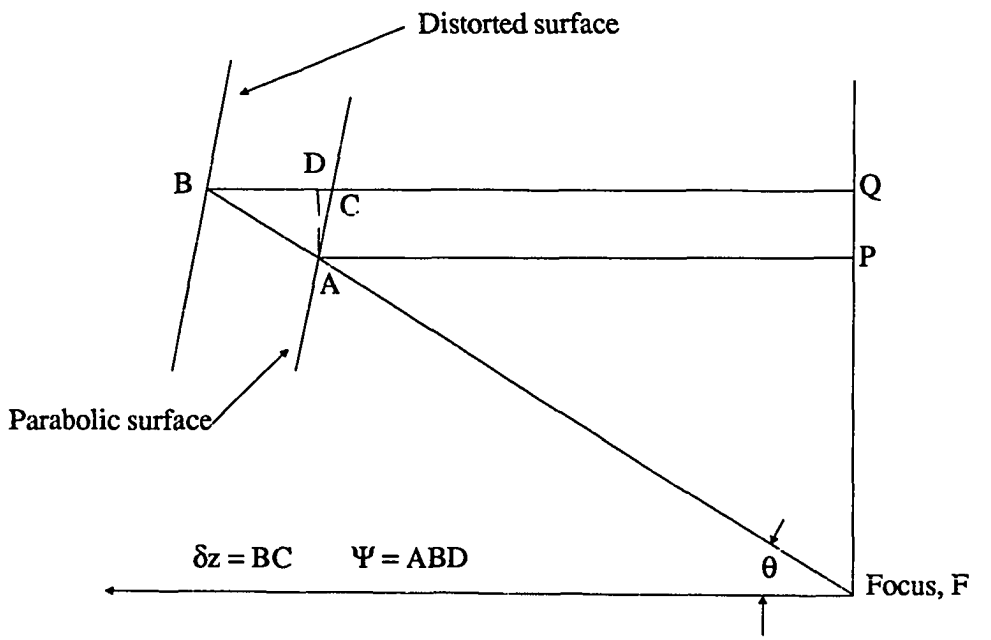

Figure 2.1-2 Relation between δz and Ψ.

Reproduced with permission of the copyright owner. Further reproduction prohibited without permission.

2.2-Control Considerations

The purpose of the control system will be to distort the surface in such a way as to improve radiometer performance; that is, to reshape the far zone field in some desired manner. In terms of the formulation of section 2.1, this means modifying the amplitudes $\vec{B}_{nm}$ and $\vec{C}_{nm}$ and phases $\vec{\beta}_{nm}$ and $\vec{\gamma}_{nm}$ due to thermal distortion. Radiometer performance requirements[3] can be stated in terms of beam efficiency, resolution, side lobe level, etc. By varying the surface shape and therefore the amplitudes and phases, any of these quantities can be controlled in theory. However, such an approach[11] leads to a nonlinear programming problem and consequently a nonlinear control problem, neither of which may be practical or necessary for real time control. An alternate approach, to be followed here, is to design a linear control system to return the far field as "close" as possible to the undisturbed field with reasonable control resources e.g. number of actuators and power.

In the following $\delta\vec{B}_{nm}$, $\delta\vec{C}_{nm}$, $\delta\Psi$, etc. are considered to be the result of both control and thermal distortions.

One measure of "close" might be $\sum_{n,m} N_{nm}\,(\,\delta\vec{B}_{nm}\cdot\delta\vec{B}_{nm} + \delta\vec{C}_{nm}\cdot\delta\vec{C}_{nm}\,)$, where

$N_{nm} = \dfrac{1+\delta_m^o}{n+1}$. This objective function is proportional to the mean square values of $\delta\vec{V}$ and $\delta\vec{W}$ since by applying Parseval's theorem to (2.1-11) and (2.1-12) yields

$$\iint_S \delta\vec{V}\cdot\delta\vec{V}\,dS = \frac{\pi}{2}\sum_{n,m} N_{nm}\,\delta\vec{B}_{nm}\cdot\delta\vec{B}_{nm} \quad \text{and} \quad \iint_S \delta\vec{W}\cdot\delta\vec{W}\,dS = \frac{\pi}{2}\sum_{n,m} N_{nm}\,\delta\vec{C}_{nm}\cdot\delta\vec{C}_{nm}.$$

Reproduced with permission of the copyright owner. Further reproduction prohibited without permission.

For the level of distortion acceptable for radiometers, $|k\delta\Psi| < \frac{\pi}{2}$ or $|\delta\Psi| < ¼$. So that

$2\sin^2\frac{k\delta\Psi}{2} < |\sin k\delta\Psi|$ and consequently $\iint_S \delta\vec{V}\cdot\delta\vec{V}dS < \iint_S \delta\vec{W}\cdot\delta\vec{W}\,dS$.

Thus $\sum_{n,m} N_{nm}\,\delta\vec{B}_{nm}\cdot\delta\vec{B}_{nm} < \sum_{n,m} N_{nm}\,\delta\vec{C}_{nm}\cdot\delta\vec{C}_{nm}$, and controlling the latter sum assures control of the former sum. To complete the process of linearizing the problem, it is assumed that $k\delta\Psi$ is sufficiently small that the small angle approximation is valid. The $\delta\vec{C}_{nm}$ are now linearly related to reflector displacements and the cost function is therefore quadratic in the displacements. The problem has now been put into a traditional control problem format; but, still no consideration has been given to the fact that the antenna distortions and therefore the $\vec{C}_{nm}$ are time dependent.

It may be very expensive, from a control system viewpoint, to control performance at all times as the radiometer orbits the Earth. In particular, during a short interval around entry into and exit from the Earth shadow there can be relatively rapid and large changes in the temperature of radiometer components. One method to reduce the over influence of such phenomena in the design of the control system is to utilize an average performance of some type. One candidate cost function is

$$\frac{1}{P}\int_0^P \sum_{n,m} N_{nm}\,\delta\vec{C}_{nm}\cdot\delta\vec{C}_{nm}\,dt,$$

where P is the orbital period.

Both of these objective functions will be discussed later and will be refered to as the Zernike-Bessel cost or J_1 and the Zernike-Bessel average cost or J_2 where

Reproduced with permission of the copyright owner. Further reproduction prohibited without permission.

$$J_1 = \sum_{n,m} N_{nm}\, \delta\vec{C}_{nm} \cdot \delta\vec{C}_{nm} = \frac{2}{\pi} \iint_S \delta\vec{W} \cdot \delta\vec{W}\, dS \tag{2.2-1}$$

and

$$J_2 = \frac{1}{P} \int_0^P J_1(t)\, dt = \frac{1}{P} \int_0^P \sum_{n,m} N_{nm}\, \delta\vec{C}_{nm} \cdot \delta\vec{C}_{nm}\, dt. \tag{2.2-2}$$

Recall that when $\Theta = 0$ for the undistorted antenna the field is given by $\vec{E}(0, 0) = \pi C\, \vec{A}_{00}$. Possible goals for the control system might be to control $\frac{J_1}{\vec{A_o} \cdot \vec{A_o}}$ and/or $\frac{J_2}{\vec{A_o} \cdot \vec{A_o}}$ to be less than 20 dB, since this would imply that the terms in equation 2.1-13 representing the antenna distortion are contributing no more than 1% of the power at the center of the beam. If t_{max} and t_{min} are the times when J_1 attains its maximum and minimum values during the orbit, then clearly $J_1(t_{min}) \le J_2 \le J_1(t_{max})$. Two approaches to account for the temporal variation come to mind and are discussed below.

First Approach:

The first approach emphasizes J_1 and calculates the temporal variations of each of the coefficients $\vec{C}_{nm}$, determines the maximum amplitude over an orbital period, and evaluates if each coefficient at its maximum value is a major contributor to the far field. This process results in the set of coefficients that must be controlled, and the control system would be designed to control this set of coefficients. In a flexible body dynamics problem, this is equivalent to determining the modes that must be controlled. The disadvantage of the direct approach is that the full set of coefficients must be evaluated at a sufficiently large number of orbital positions that the maximum of each coefficient can be determined. The far zone field can be calculated from equation 2.1-13

Reproduced with permission of the copyright owner. Further reproduction prohibited without permission.

$$\vec{E}=2\pi C\sum_{n}\frac{J_{n+1}(\gamma)}{\gamma}\sum_{m}j^{m}\,(1+\delta_{m}^{o})(-1)^{\frac{n-m}{2}}\times$$

$$\{\vec{A}_{nm}\cos m(\Phi-\vec{\alpha}_{nm})-\vec{B}_{nm}\cos m(\Phi-\vec{\beta}_{nm})-j\vec{C}_{nm}\cos m(\Phi-\vec{\gamma}_{nm})\}.$$

where $\gamma = ka\sin\Theta$ and the coefficients are determined by integrals over the aperture from equations (2.1-15 to -17), and in particular:

$$\vec{C}_{nm}(t)\,e^{j\vec{\gamma}_{nm}(t)}=\frac{2}{\pi N_{nm}}\int_{0}^{2\pi}\int_{0}^{1}\vec{W}(\tau,\varphi,t)\,R_{nm}(\tau)\,e^{jm\varphi}\,\tau\,d\tau\,d\varphi,$$

where the linearized version (2.1-12) of $\vec{W}$ is used, i.e. $\vec{W}(\tau,\varphi,t)=\vec{u}\sqrt{G}\,k\,\Psi(t)\cos\theta/2$ which is now considered to be a function of time, t. The only term in $\vec{W}$ that is time dependent is Ψ, that is, the phase error in the aperture plane. The temporal variation $\vec{C}_{nm}(t)$ can be determined from the integral. For each coefficient there will be a time when the coefficient reaches its maximum absolute value, say t_{nm}.

Since, for $n>0$, $\left|\frac{J_{n+1}(\gamma)}{\gamma}\right|\le 1$, the maximum relative power that any term can contribute is $\frac{\vec{C}_{nm}(t_{nm})\cdot\vec{C}_{nm}(t_{nm})}{\vec{A}_{00}\cdot\vec{A}_{00}}$. Selecting terms to control can be based on a specified dB level of say -20 or -30 dB.

An alternate version of an approach that emphasizes the Zernike- Bessel cost J_1 is to start with equation 2.2-1: $J_1=\frac{2}{\pi}\iint_{S}\delta\vec{W}\cdot\delta\vec{W}\,dS$. Under the assumption of small phase errors, this approach is similiar to minimizing RMS surface distortion except that it would generalize the RMS approach to include polarization and feed taper with only a modest

Reproduced with permission of the copyright owner. Further reproduction prohibited without permission.

increase in computational cost. But, like previous results[9], there is still the difficulty of handling the temporal effect.

Second Approach:

The second approach, which emphasizes the Zernike-Bessel average cost from equation 2.2-2, will be the major focus of this work because the temporal variations can be readily included in the development of optimal actuator locations and control laws. A principal component approach is used to decompose the linearized version of $\vec{W}$ into spatial and temporal components. Principal component analysis has a long history, spanning almost a century, and has been applied to a number of diverse fields including geometry[17], statistics[18], matrix theory[19], and meteorology.[20] It has been extensively applied in geophysical data analysis[21] and has recently been applied to control theory.[22] The salient feature of principal component analysis, as used in the latter two applications, is the ability to decompose a time dependent spatial vector field into components that are both spatially and temporally orthogonal.

For a sufficiently large number of points (τ_i, φ_i), $i = 1,..., N$ suitably distributed over the aperture plane $0 \le \tau \le 1$, $0 \le \varphi \le 2\pi$, the quadrature for $\vec{C}_{nm}$ (2.1-17) can be approximated by

$$\vec{C}_{nm}(t)\, e^{j\vec{\gamma}_{nm}(t)} \approx \frac{2}{\pi N_{nm}} \sum_{i=1}^{N} \vec{W}(\tau_i, \varphi_i, t)\, R_{nm}(\tau_i)\, e^{jm\varphi_i}\, \Delta S, \tag{2.2-3}$$

where $\Delta S = \tau_i\, d\tau_i\, d\varphi_i = \pi/N$ is independent of i. With such a set of points, form the N by 3 matrix

Reproduced with permission of the copyright owner. Further reproduction prohibited without permission.

$$G(t) = \begin{bmatrix} W_x(\tau_1, \varphi_1, t), & W_y(\tau_1, \varphi_1, t), & W_z(\tau_1, \varphi_1, t) \\ W_x(\tau_2, \varphi_2, t), & W_y(\tau_2, \varphi_2, t), & W_z(\tau_2, \varphi_2, t) \\ \cdot & \cdot & \cdot \\ \cdot & \cdot & \cdot \\ W_x(\tau_N, \varphi_N, t), & W_y(\tau_N, \varphi_N, t), & W_z(\tau_N, \varphi_N, t) \end{bmatrix}, \tag{2.2-4}$$

where W_x is the x component of $\vec{W}$, etc.

The following development of the principal components and their properties is specialized to the problem at hand, but follows the development of Moore.[22] Form the Grammian matrix:

$$H = \frac{1}{P}\int_0^P G(t)\, G^T(t)\, dt, \tag{2.2-5}$$

where P is the orbital period. H is a symmetric, positive semi-definite matrix with non-negative "principal eigenvalues" $\sigma_1^2 \geq \sigma_2^2 \ldots \geq \sigma_N^2 \geq 0$ and real, orthogonal, unit "principal eigenvectors" $\vec{e_1}, \vec{e_2}, \ldots, \vec{e_N}$.

G can be expanded in terms of the eigenvectors as $G = \sum_{i=1}^{N} e_i\, g_i^T(t)$ (2.2-6)

where

$$g_i(t) = G^T(t)\, e_i \tag{2.2-7}$$

is a 3 by 1 matrix of the projection of the three columns of G onto the eigenvectors and e_i is the N by 1 matrix form of the eigenvector $\vec{e_i}$. The $g_i(t)$ are called the "principal component amplitudes." In what follows interchanging between vector and matrix notation will take place without further comment. Equation 2.2-6 is therefore an expansion of G in a set of time dependent, spatially orthogonal "principal components" $e_i\, g_i^T(t)$.

Reproduced with permission of the copyright owner. Further reproduction prohibited without permission.

If the above expansion for G is substituted into equation 2.2-5 one obtains

$$H = \frac{1}{P}\int_0^P \left\{ \sum_{i=1}^{N}\sum_{j=1}^{N} e_i\, g_i^T(t)\, g_j(t)\, e_j^T \right\} dt = \sum_{i=1}^{N}\sum_{j=1}^{N} e_i \left\{ \frac{1}{P}\int_0^P g_i^T(t)\, g_j(t)\, dt \right\} e_j^T .$$

Premultiply by e_p^T and postmultiply by e_q and use the orthogonality of the eigenvectors to get

$$\frac{1}{P}\int_0^P g_p^T(t)\, g_q(t) dt = e_p^T H\, e_q = e_p^T\, \sigma_q^2\, e_q = \sigma_q^2 e_p^T\, e_q = \sigma_q^2\, \delta_p^q . \tag{2.2-8}$$

The principal component amplitude vectors $g_i(t)$ are therefore orthogonal in time.

It is convenient to collect the eigenvectors as columns in an N by N matrix E and the component amplitudes as rows in a N by 3 matrix G_e so that

$$G = E\, G_e . \tag{2.2-9}$$

For later reference note that

$$\|G\|^2 = \|G_e\|^2 = \sum_{i=1}^{N} g_i^T\, g_i \quad . \tag{2.2-10}$$

To obtain an approximate relation between the eigenvalues, the coefficients C_{nm} and the objective functions without control start with

$$\|G\|^2 = \text{trace}\; G\, G^T = \sum_{i=1}^{N} \vec{W}(\tau_i, \varphi_i, t)\cdot\vec{W}(\tau_i, \varphi_i, t) \approx \frac{N}{\pi}\int_0^{2\pi 1}\int_0 \vec{W}(\tau, \varphi, t)\cdot\vec{W}(\tau, \varphi, t)\, \tau\, d\tau\, d\varphi .$$

Reproduced with permission of the copyright owner. Further reproduction prohibited without permission.

But from above, $\int\int \vec{W} \cdot \vec{W}\, \tau\, d\tau\, d\varphi = \frac{\pi}{2} \sum_{n,m} N_{nm}\, \vec{C}_{nm} \cdot \vec{C}_{nm} = \frac{\pi}{2} J_1$. Thus, $J_1 \approx \frac{2}{N} \|G\|^2$.

$$\text{Also, } \sum_{n=1}^{N} \sigma_i^2 = \text{trace } H = \frac{1}{P} \int_0^P \text{trace } GG^T\, dt \approx \frac{N}{2P} \int_0^P \sum_{n,m} N_{nm}\, \vec{C}_{nm}(t) \cdot \vec{C}_{nm}(t)\, dt = \frac{N}{2} J_2.$$

So the two Zernike-Bessel costs have been related to the G matrix and the eigenvalues of the Grammian:

$$J_1 \approx \frac{2}{N} \|G\|^2 = \frac{2}{N} \sum_{i=1}^{N} g_i^T g_i \tag{2.2-11}$$

and

$$J_2 \approx \frac{2}{N} \sum_{i=1}^{N} \sigma_i^2 = \frac{1}{P} \int_0^P J_1(t)\, dt. \tag{2.2-12}$$

One of the rationales for using the principal component decomposition is the expectation that the eigenvalues decrease rapidly so that the cost J_2 is dominated by a small number of the largest eigenvalues. In this case, the control system design would be reduced to controlling only the far field distortion due to the eigenfunctions corresponding to the reduced set.

To develop a criteria for selecting the significant eigenvalues consider the first term in the Zernike-Bessel expansion $\vec{A}_{00}$ (2.1-14) which determines the far field at the center of the beam for an undistorted antenna:

$$\vec{A}_{00} = \frac{1}{\pi} \int_0^{2\pi} \int_0^1 \vec{U}(\tau, \varphi)\, \tau\, d\tau\, d\varphi. \tag{2.2-13}$$

Reproduced with permission of the copyright owner. Further reproduction prohibited without permission.

If $\frac{J_2}{\left|\vec{A}_{00}\right|^2} << 1$ then the distortions of the far field averaged over an orbital period will be negligible. But, $\frac{J_2}{\left|\vec{A}_{00}\right|^2} = \frac{2}{N}\sum \frac{\sigma_i^2}{\left|\vec{A}_{00}\right|^2}$. Thus, it is only necessary to consider those eigenvalues that contribute some preset limit, say -30 dB, in the control system design. The influence of the omitted principle components must, of course, be evaluated after the system is designed.

2.3-Actuator Control Laws and Locations

In section 2.2, methods were discussed for selecting the coefficients $\vec{C}_{nm}(t)$ or the principal components eig_i^T to be controlled. The emphasis here will be on the latter set, i.e. the principal components of the thermal distortion field. Given this set, the next question is how many actuators should be used, where should they be located, and how should they be controlled? In what follows the objective function will be $\|\delta G\|^2$, where δG is the difference between the G matrices due to thermal and control distortions.

Open Loop Control With Actuators Fixed

First consider the design of an open loop control when the actuator locations are known. Assume there are M actuators at preselected sites. For the α-th actuator $\alpha=1,...,M$ a unit stroke will produce a reflector surface displacemant field which can be converted to a phase function $\Psi_\alpha(\tau, \varphi)$ and then to a $\vec{W}_\alpha(\tau, \varphi)$ field. As was done above for the thermal distortion field, the control field can be discretized to form a N by 3 matrix for each of the M actuators

Reproduced with permission of the copyright owner. Further reproduction prohibited without permission.

$$G_\alpha = \begin{bmatrix} W_{\alpha_x}(\tau_1, \varphi_1), & W_{\alpha_y}(\tau_1, \varphi_1), & W_{\alpha_z}(\tau_1, \varphi_1) \\ W_{\alpha_x}(\tau_2, \varphi_2), & W_{\alpha_y}(\tau_2, \varphi_2), & W_{\alpha_z}(\tau_2, \varphi_2) \\ \cdot & \cdot & \cdot \\ \cdot & \cdot & \cdot \\ W_{\alpha_x}(\tau_N, \varphi_N), & W_{\alpha_y}(\tau_N, \varphi_N), & W_{\alpha_z}(\tau_N, \varphi_N) \end{bmatrix}, \tag{2.3-1}$$

where W_{α_x} is the x component of $\vec{W}_\alpha$, etc.

Each of these matrices is decomposed into components along the principal eigenvectors to get

$$G_\alpha = \sum_{i=1}^{N} e_i f_{\alpha i}^T = E\, F_{e_\alpha}, \tag{2.3-2}$$

where $f_{\alpha i} = G_\alpha^T e_i$ is 3 by 1 and $F_{e_\alpha} = E^T G_\alpha$ is N by 3, $\quad \alpha = 1...M$.

Let s_α represent the the stroke of the α-th actuator. As stated above, the goal is to select a set of s_α so that the difference, δG, between the surface thermal distortion and the actuator induced distortions has minimum norm, that is, minimize

$$\|\delta G\| \equiv \left|\left| G - \sum_{\alpha=1}^{M} s_\alpha G_\alpha \right|\right|. \tag{2.3-3}$$

Minimizing $\|\delta G\|^2$, which will minimize the cost J_1 (2.2-11), is thus a classical least square problem of finding the M values of s_α that minimize the sum of squares of the elements in the δG matrix. Setting $\frac{\partial \|\delta G\|}{\partial s_\alpha} = 0$ for each $\alpha = 1,...,M$ leads to the system of equations

Reproduced with permission of the copyright owner. Further reproduction prohibited without permission.

$$\begin{bmatrix} (G_1.*G_1), & (G_2.*G_1), & \cdot\ \cdot & (G_M.*G_1) \\ (G_1.*G_2), & (G_2.*G_2), & \cdot\ \cdot & (G_M.*G_2) \\ \cdot & \cdot & \cdot\ \cdot & \cdot \\ \cdot & \cdot & \cdot\ \cdot & \cdot \\ (G_1.*G_M), & (G_2.*G_M), & \cdot\ \cdot & (G_M.*G_M) \end{bmatrix} \begin{vmatrix} s1 \\ s2 \\ \cdot \\ \cdot \\ sM \end{vmatrix} = \begin{vmatrix} (G.*G_1) \\ (G.*G_2) \\ \cdot \\ \cdot \\ (G.*G_M) \end{vmatrix}, \tag{2.3-4}$$

where $(A.*B)$ is a short hand notation for the sum of the element by element products of A and B, e.g. $\|A\|^2 = (A.*A)$.

Since the coefficient matrix is a function of only the actuator locations and can be pre-inverted, this set of equations would be convenient for real time control. The right hand side vector can be calculated from either M stored G_α matrices or can be written as a N by N matrix times the phase error Ψ at the N points. The solution gives $\hat{s}$ from which the minimum cost at each time $J\hat{\uparrow} = \frac{2}{N}\|\delta\hat{G}\|^2$ can be determined.

However, in order to relate the solution directly to the cost, it is convient to also solve the equations in principal component form. From 2.2-9 and 2.3-2 write

$$\delta G = E\,G_e - \sum_{\alpha=1}^{M} s_\alpha\, EF_{e_\alpha} = E\left[G_e - \sum_{\alpha=1}^{M} s_\alpha\, F_{e_\alpha}\right].$$

For any matrix Y, $\|Y\|^2 = tr\ YY^T = tr\ Y^TY$, so that

$$\|\delta G\|^2 = tr\left[E\{G_e - \sum_{\alpha=1}^{M} s_\alpha\, F_{e_\alpha}\}\right]^T\left[E\{G_e - \sum_{\alpha=1}^{M} s_\alpha\, F_{e_\alpha}\}\right]$$

Since $E^T E = I$,

Reproduced with permission of the copyright owner. Further reproduction prohibited without permission.

$$\|\delta G\|^2 = tr\left[G_e - \sum_{\alpha=1}^{M} s_\alpha F_{e_\alpha}\right]^T \left[G_e - \sum_{\alpha=1}^{M} s_\alpha F_{e_\alpha}\right] = \left|\left|G_e - \sum_{\alpha=1}^{M} s_\alpha F_{e_\alpha}\right|\right|^2.$$

From the form of this equation, it is seen that the solution will give the s_α as linear combinations of the components of G_e, which are the time dependent amplitudes of the principal components. Consequently, the open loop optimal control for each actuator will be a linear combination of the principal component amplitudes. Clearly minimizing J_1 at each time will minimize J_2.

To put the above expressions into a standard least square format, form the 3N vector y, the 3N by M matrix F and the M vector s :

$$y = \begin{vmatrix} g1 \\ g2 \\ \cdot \\ \cdot \\ gN \end{vmatrix} \quad F = \begin{bmatrix} f1_1, f2_1, \cdots fM_1 \\ f1_2, f2_2, \cdots fM_2 \\ \cdot \quad \cdot \quad \cdots \quad \cdot \\ \cdot \quad \cdot \quad \cdots \quad \cdot \\ f1_N, f2_N, \cdots fM_N \end{bmatrix} \quad s = \begin{vmatrix} s1 \\ s2 \\ \cdot \\ \cdot \\ sM \end{vmatrix}. \tag{2.3-5}$$

In this notation, $\|\delta G\| = \| y - F\, s \|$, with the least square solution $\hat{s}$ given by

$$\hat{s} = \left[F^T F\right]^{-1} F^T y. \tag{2.3-6}$$

The minimum norm is $\|\delta \hat{G}\|^2 \equiv \| y - F\, \hat{s} \|^2 = y^T \left[I - F(F^T F)^{-1} F^T\right] y.$

$$\text{Let } P = I - F(F^T F)^{-1} F^T. \tag{2.3-7}$$

P is the idempotent projection associated with the least square estimator, so

$$J_1 = \frac{2}{N} \|\delta \hat{G}\|^2 = \frac{2}{N} y^T P y. \tag{2.3-8}$$

Reproduced with permission of the copyright owner. Further reproduction prohibited without permission.

In the case of a linearily polarized aperture pattern, both G and G_α are vectors and an explicit relation between the minimum norm and the eigenvalues can be obtained, since

when $y(i) = g_i$ then $\|\delta\hat{G}\|^2 = \sum_{i=1}^{N}\sum_{j=1}^{N} g_i P(i,j) g_j$.

Form the integral over the period and recall (2.2-8), $\frac{1}{P}\int_0^P g_i{}^T g_j \, dt = \sigma_i^2 \delta_i^j$, so that

$$J_2 = \frac{2}{NP}\int_0^P \|\delta\hat{G}\|^2 dt = \sum_{i=1}^{N}\sum_{j=1}^{N} \frac{2}{NP}\int_0^P g_i P(i,j) g_j \, dt = \sum_{i=1}^{N} \sigma_i^2 P(i,i). \tag{2.3-9}$$

Open Loop Control & Actuators Free To Move:

The optimal location of sensors and/or actuators is a fundamental problem in control, system identification and state estimation. A survey[23] of current methods demonstrates that no general solution to the problem exists and existing approximate techniques have various inadequacies. The problem of locating sensors or actuators usually influences the cost or objective function through the inverse of a matrix. When the locations are discrete, changing a location means changing a row and/or column of the matrix and then reinverting. Thus in addition to the exponential explosion in combinations with the number of possible sites, testing a new site requires a large matrix inverse. There are no general methods for obtaining the new inverse without actually performing the complete numerical inverse. Specifically, for the problem at hand, changing an actuator location changes the F matrix (2.3-5), which influences the cost through the P matrix, which requires inverting $F^T F$. Approximate solutions will be discussed below.

Reproduced with permission of the copyright owner. Further reproduction prohibited without permission.

If there are K possible sites for M identical actuators, there are $\frac{K!}{(K-M)!\,M!}$ distinct configurations of actuators. To select among all these configurations requires the definition of optimal. Two obvious candidates are to minimize J_2 or to minimize the maximum value over time of J_1. In the general case, both of these candidates have the problem discussed above.

To minimize J_2, first perform the one time quadrature $Y(i,j) = \frac{1}{P}\int_0^P y(i)\,y(j)\,dt$ as suggested by equation 2.3-8. If the eigenvalues decrease rapidly, then $|Y(i,j)|$ should also decrease rapidly with i and j since by Cauchy's inequality:

$$\left[\frac{1}{P}\int_0^P y(i)\,y(j)\,dt\right]^2 \le \left[\frac{1}{P}\int_0^P y^2(i)\,dt\right]\left[\frac{1}{P}\int_0^P y^2(j)\,dt\right] \le \left[\frac{1}{P}\int_0^P |g_{k_i}|^2\,dt\right]\left[\frac{1}{P}\int_0^P |g_{k_j}|^2\,dt\right] = \sigma_{k_i}^2\,\sigma_{k_j}^2,$$

where the second inequality holds because $y(i)$ is one of the three components of g_{k_i}.

The Zernike-Bessel average cost can thus be written as

$$J_2 = \frac{2}{NP}\sum_{i=1}^{3N}\sum_{j=1}^{3N}\int_0^P y(i)\,P(i,j)\,y(j)dt = \frac{2}{N}\sum_{i=1}^{3N}\sum_{j=1}^{3N} Y(i,j)\,P(i,j). \qquad (2.3\text{-}10)$$

For the linearly polarized case $J_2 = \frac{2}{N}\sum_{i=1}^{N}\sigma_i^2\,P(i,i)$ (2.3-11)

In either case, the remaining problem is a discrete optimization problem with no known algorithm to obtain the optimum except exhaustive search. In this case, $\frac{K!}{(K-M)!\,M!}$ projection matrices P must be calculated, each of which involves the inverse of a M by M

Reproduced with permission of the copyright owner. Further reproduction prohibited without permission.

matrix. Generally it is also desirable to determine the minimum number of actuators that will satisfy some antenna performance criteria, so the optimal must be determined for a number of values of M as well.

Though there are numerous theoretical papers[23] on optimal sensor and actuator location, there are in fact few methods. Many of the methods[10] are substitution approaches wherein the least effective occupied location and the most effective unoccupied location are identified and interchanged until there is no improvement in the objective. There are also approaches[24] where all locations are initialized as occupied (unoccupied) and then the least (most) effective location is removed (occupied).

For the objective $J_2 = \frac{2}{N}\sum_{i=1}^{3N}\sum_{j=1}^{3N} Y(i,j)\,P(i,j)$ it is possible to develop a method that optimally adds an additional actuator. Let $\boldsymbol{P}$ and $\boldsymbol{F}$ correspond to some actuator configuration and $\boldsymbol{P}_+$ and $\boldsymbol{F}_+$ be the same configuration with one additional actuator. The task is to find an expression for $\boldsymbol{P}_+$ that does not require a new matrix inverse. The required expression can be developed from the well known relation for partitioned symmetric matrices:

$$\begin{vmatrix} \boldsymbol{A} & \boldsymbol{B} \\ \boldsymbol{B}^T & \boldsymbol{C} \end{vmatrix}^{-1} = \begin{vmatrix} \boldsymbol{A}^{-1}+\boldsymbol{A}^{-1}\boldsymbol{B}(\boldsymbol{C}-\boldsymbol{B}^T\boldsymbol{A}^{-1}\boldsymbol{B})^{-1}\boldsymbol{B}^T\boldsymbol{A}^{-1}, & -\boldsymbol{A}^{-1}\boldsymbol{B}(\boldsymbol{C}-\boldsymbol{B}^T\boldsymbol{A}^{-1}\boldsymbol{B})^{-1} \\ -(\boldsymbol{C}-\boldsymbol{B}^T\boldsymbol{A}^{-1}\boldsymbol{B})^{-1}\boldsymbol{B}^T\boldsymbol{A}^{-1}, & (\boldsymbol{C}-\boldsymbol{B}^T\boldsymbol{A}^{-1}\boldsymbol{B})^{-1} \end{vmatrix}.$$

Write $\boldsymbol{F}_+ = |\ \boldsymbol{F},\ \boldsymbol{f}\ |$, where $\boldsymbol{f}$ is the additional column to be appended to $\boldsymbol{F}$ for the additional actuator. Before applying the expression above to $(\boldsymbol{F}_+^T\boldsymbol{F}_+)^{-1}$ note that the term corresponding to $\boldsymbol{C}-\boldsymbol{B}^T\boldsymbol{A}^{-1}\boldsymbol{B}$ is a scalar and can be written as $\boldsymbol{f}^T\boldsymbol{P}\boldsymbol{f}$, thus

Reproduced with permission of the copyright owner. Further reproduction prohibited without permission.

$$(F_+^T F_+)^{-1} = \begin{vmatrix} F^T F, & f^T F \\ F^T f, & f^T f \end{vmatrix}^{-1} = \begin{vmatrix} (F^T F)^{-1} + \dfrac{(F^T F)^{-1} F^T f f^T F (F^T F)^{-1}}{f^T P f}, & \dfrac{-(F^T F)^{-1} F^T f}{f^T P f} \\ \dfrac{-f^T F (F^T F)^{-1}}{f^T P f}, & \dfrac{1}{f^T P f} \end{vmatrix}.$$

Direct substitution leads to

$$P_+ = P + \frac{P f f^T P^T}{f^T P f}. \tag{2.3-12}$$

It is seen that after the 3N vector Ff is formed, calculating P_+ from P only requires 1 vector outer product and 1 vector inner product. Even fewer calculations are required for a linearily polarized antenna where only the trace of P_+ is required.

Given any configuration of actuators, the above equations provide the basis for identifying the most effective actuator for augmentation of the configuration. For large structures there may be a large variety of sites and it would therefore be convenient to restrict the total set to a smaller subset of the "most effective" sites prior to beginning the above search technique. Recall that for the linearily polarized case $J_2 = \frac{\pi}{N} \sum_{i=1}^{N} \sigma_i^2 P(i,i)$. Suppose that the sensitivity matrix for each of the actuators G_α, a vector for this case, is a linear combination of only the eigenvectors corresponding to the L largest eigenvalues. Then $f_{\alpha_i} = 0$ for i = L+1, L+2,...N, and so F_{e_α} has the form

$F_{e_\alpha} = \begin{vmatrix} F_L \\ 0 \end{vmatrix}$, where F_L is an L by L matrix which is assumed to have an inverse so that the s_α have a solution. In this case, $P = I - \begin{vmatrix} F_L (F_L{}^T F_L)^{-1} F_L{}^T, & 0 \\ 0, & 0 \end{vmatrix} = \begin{vmatrix} 0 & 0 \\ 0 & I \end{vmatrix}$

Reproduced with permission of the copyright owner. Further reproduction prohibited without permission.

So that, $J_2 = \frac{\pi}{N}\sum_{i=L+1}^{N} \sigma_i^2$. The L largest eigenvalues are therefore excluded from the cost, and it can be shown[22] that this is the absolute minimum cost for any L actuators. The result does not extend easily to the general polarization case, but does suggest that a criteria for ordering potential actuator sites is the "effectiveness" ratio

$$\varepsilon_\alpha \equiv \frac{\sum_{i=1}^{L} f_{\alpha i}^T f_{\alpha i}}{\sum_{i=1}^{N} f_{\alpha i}^T f_{\alpha i}} = \frac{\sum_{i=1}^{L} f_{\alpha i}^T f_{\alpha i}}{\|G_\alpha\|^2} = \frac{\|F_{\alpha L}\|^2}{\|G_\alpha\|^2}, \tag{2.3-13}$$

where $F_{\alpha L} = G_\alpha^T E_L$ and E_L is the N by L matrix of the first L eigenvalues. Also, $\sum_{i=1}^{N} f_{\alpha i}^T f_{\alpha i} = \|F_{e_\alpha}\|^2 = \|G_\alpha\|^2$ has been used in the denominator. The effectiveness is a relative measure of the extent to which the α-th sensitivity matrix can be represented as a linear combination of the first L eigenvectors. If $\varepsilon_\alpha = 1$ then the columns of G_α are vectors in the hyperplane determined by the first L eigenvectors, and the first L principal components can be controlled without "exciting" the remaining principal components. On the other hand, if $\varepsilon_\alpha = 0$ then the columns of G_α are orthogonal to the hyperplane. In the latter case locating actuators at such sites can contribute nothing to reducing the contribution of the first L eigenvalues to J_2.

Even though ε_α provides a means of ordering the possible actuator location sites, care must be exercised in the use of such an ordering. If two sites could produce the same G_α they would have the same ε_α but including both in the potential site list is clearly redundant. The goal is to pick actuator sites that are effective as measured by ε_α and mutually

Reproduced with permission of the copyright owner. Further reproduction prohibited without permission.

orthogonal. One measure of orthogonality, to be used later, is the rod "correlation factor" for two actuator sites α and β

$$\varepsilon_{\alpha\beta} \equiv \frac{\sum_{i=1}^{L} f_{\alpha_i}^T f_{\beta_i}}{\|F_{\alpha_L}\| \, \|F_{\beta_L}\|}. \tag{2.3-14}$$

2.4-Processing Sensor Data

In section 2.3 an open loop control law was developed that minimized the norm of $\delta G = G - \sum_{\alpha=1}^{M} s_\alpha G_\alpha$ and a method was presented for obtaining the optimal set of actuator locations which define the matrices G_α. If perfect models existed for predicting the antenna distortion then an open loop system would be adequate for controlling the far field. However, there are many potential sources of uncertainties in these models. To account for such errors a closed loop system, which relies on measurements to determine deviations from the nominal state, will be required normally.

It is assumed that the fundamental measurements are measurements of displacements of the reflecting surface in the z direction. Such measurements can be provided by reflecting laser beams off of corner cubes attached to the surface. The question then becomes how many reflectors (sensors) are required, where to place them on the surface and how to feed back these data to control the distortion?

First, convert these measurements to equivalent aperture plane phase shift using equation 2.1-8. It is assumed that the possible sensor sites are on the reflector surface and, without loss of generality, are some subset of the N surface locations used to discretize the perturbed electric field integral (2.2-3). Sensors could be placed at other points; but, then a

Reproduced with permission of the copyright owner. Further reproduction prohibited without permission.

transformation would be required to convert the measurement to an aperture plane phase shift. However, with such a transformation the methods discussed herein are directly applicable.

In the ideal situation the phase shift would be measured at all points in the aperture plane; unfortunately, this would take an excessive number of sensors. On the other hand with a few sensors large errors can result during extrapolation to the global shape. The heart of the optimal sensor location problem is selecting the minimum number and locations so that the extrapolation error is acceptable. The use of cubic splines has received much attention for this purpose; but, for the problem at hand, the principal component eigenvectors provide a natural basis for extrapolation. The sensor information will consequently be used to directly estimate the principle component amplitudes as defined by equation 2.2-7. The approach taken here will thus be to select sensor locations that provided the best estimate of the principal component amplitudes. As a result of this approach the absolute minimum number of sensors will be found below and the minimum number required to meet peformance requirements will be found in the usual parametric search manner. Once the principal component amplitudes have been estimated, an estimate $\hat{G}$ of G can be made using equation 2.2-6. Then the actuator strokes s_α will be selected, using equation 2.3-4, to minimize the norm of $\delta G = \hat{G} - \sum_{\alpha=1}^{M} s_\alpha G_\alpha$, where $\hat{G}$ is an estimate of G obtained from the sensors.

Before formulating an estimator for G, note that the three columns of G are not independent, since they are just the three components of $\vec{W}$, which are related by the three components of $\vec{u}$ through equation 2.1-12. Thus if one component is known the other two can be calculated. Conversely, there is only a need to estimate the amplitude corresponding to one column of the G matrix. For example, if the y-component is selected,

Reproduced with permission of the copyright owner. Further reproduction prohibited without permission.

equation 2.2-9, $G = E\,G_e$, reduces to $\vec{W}_y = E\,\vec{g}_y$. Since the chosen component is arbitrary, the y subscript will be dropped in the following. The observation equation is therefore

$$\vec{W} = E\,\vec{g}. \tag{2.4-1}$$

If one had measurements of aperture phase Ψ at all N points the full $\vec{W}$ would be known and the full magnitude vector $\vec{g}$ could be calculated. In practice, sensors are not placed at all N points. Further, estimating all components of the amplitude vector is not required since some components will not contribute to errors in the far field.

Let S be the number of sensors on the surface. Convert the measurement at each sensor into aperture plane phase and then into $\vec{W}$ form, as assumed above. With these S measurements form the S vector, $\vec{W}_s$. With only S measurements it will not be possible to estimate all N components of $\vec{g}$, so select P < S of the columns of E to form the N by P matrix E_p. From this matrix select the rows corresponding to the sensor locations to form the S by P sub-matrix E_{sp}. The relation between the measurements $\vec{W}_s$ and the unknown amplitudes $\vec{g}_p$ becomes the observation equation

$$\vec{W}_s = E_{sp}\,\vec{g}_p \tag{2.4-2}$$

The magnitudes of the "significant" principal components, that is, the components that have principal eigenvalues that are sufficiently large to contribute to unacceptable far field errors, must be estimated. Assuming that it is possible to identify significant components, the minimum number of sensors is therefore equal to the number of significant principal components. Recognizing that there are measurement errors in $\vec{W}_s$, equation 2.4-2 becomes a classical estimation problem with well known solution

Reproduced with permission of the copyright owner. Further reproduction prohibited without permission.

$$\hat{g}_p = [\, E_{sp}^T \Gamma^{-1} E_{sp} \,]^{-1} E_{sp}^T \Gamma^{-1} \vec{W}_s, \tag{2.4-3}$$

where Γ is the covariance on the measurement vector $\hat{W}_s$, which is readily calculated from the covariance on the fundamental measurements of surface displacement. It is especially important to include this term for highly tapered feeds.

Once an estimate $\hat{g}_p$ is obtained, the estimate of the entire column W of G is obtained from

$$\hat{W} = E_p \hat{g}_p. \tag{2.4-4}$$

and the other two columns of G can be calculated as mentioned above to give the final estimate $\hat{G}$, which will be used in equation 2.3-4 to obtain the optimal actuator strokes.

The remaining problem is how many sensors to place on the surface and where to place them. Like the optimal actuator location problem this is a discrete optimization problem and there are a number of discrete optimization approaches[23] for solving the problem as formulated above.

Reproduced with permission of the copyright owner. Further reproduction prohibited without permission.

Chapter 3-Validation Studies

In this chapter the theory developed in Chapter 2 will be tested using a typical large space radiometer model. Since there are no experimental results against which the theory can be tested, a number of simulations have been generated to define limits of applicability and areas for future improvements.

3.1-Selection of Validation Model

Radiometer and Orbit Parameters

The 55-meter tetrahedral truss (figure 3.1-1) studied by Haftka[9] and by Padula[11] was selected as the antenna against which to test the theory developed in Chapter 2 and to validate some of the concepts. Appendix B shows the antenna geometry and illustrates grid and rod locations. The original design[25] was based on a material with a Young's modulus of 2.6×10^{11} N/m^2 (37×10^6 psi) and a clamped-clamped rod buckling load of 4000-N (900-lbs). This leads to the 8-m long tubes on the front and back faces of the antenna having a diameter of 4-cm and wall thickness of 0.1-cm. A more conservative modulus, currently used for designing operational spacecraft like Space Station Freedom, of 1.1×10^{11} (16×10^6 psi) will be used for this study. For an actively controlled structure, the members must be able to support the stresses produced by the actuators. Based on nominal values of structural and thermal properties, structrual deformations are expected to be in the millimeter range. So one might expect actuator strokes in the same range. The equivalent compressive force for a constrained rod would be about 2000 N, which

Reproduced with permission of the copyright owner. Further reproduction prohibited without permission.

cannot be met with the reduced modulus. Consequently, the diameter of all the rods was increased to 5 cm and the thickness maintained at 0.1 cm. thereby providing a 75% buckling safety margin for 1 mm strokes.

The orbit geometry studied is a geosynchronous orbit (GEO). The 55-meter antenna can not meet all the science requirements specified in Table 3 of reference 3, but would provide adequate resolution for sensing atmospheric water vapor, rain and clouds, which require frequencies between 15 and 31 GHz. Sensing soil moisture, sea surface temperature, and salinity requires lower frequencies and higher resolution, both of which mean a larger radiometer. The 55-meter antenna will, nevertheless, generically exhibit all the thermal, structural, RF, and control characteristics of a larger antenna. The z-axis of the antenna (figure 2.1-1) points directly away from the center of the earth with the y-axis normal to the orbit plane in the same direction as the orbital angular momemtum vector.

Thermal Effects During the Orbit

The temperature at any point on the antenna is determined by conduction and radiation among the components of the antenna and from the radiant energy received from the Earth and the Sun. Deviations in temperature from the design temperature lead to thermal distortions which can be determined by thermal analysis[26] and/or by thermal/vacuum testing. For the purposes of calculating these distortions, it is assumed that a knitted mesh is supported on the truss structure to reflect radio frequency waves. Knitted meshes are isotropic membranes that conform to a minimal surface[27] so the surface shape is solely a function of the boundary shape. Attachment of the mesh at only the node points, which are 8 meters apart, would lead to unacceptable deviations from the desired parabolic shape.[28] Thus, a system of tie downs will be required to constrain the mesh. The tie downs may also undergo thermal distortions; however, the result of such distortions will

Reproduced with permission of the copyright owner. Further reproduction prohibited without permission.

depend on the details of the tie down geometry. For this study, it is assumed that the triangle of mesh between structural nodes behaves like a rigid surface and that this surface translates with the nodal displacements at the three corners. The displacement of any point on the mesh is thus a linear combination of the displacements of the three truss nodes surrounding the point.

Thermal analyses[26] of space trusses of this type show that conduction and intra-antenna radiation are of secondary importance when compared to direct solar and terrestial radiative heating and radiative cooling to deep space. Consequently, for the purposes here it will be assumed that each rod in the antenna structure is isothermal and the radiative input only depends on its orientation with respect to the Earth and Sun. The solar flux q_S is taken to be 1380 $^{W}/_{m^2}$ and is modeled as a point source at infinity. The emitted radiation from the top of the earth atmosphere q_e is 241 $^{W}/_{m^2}$.[29] The temperature of each rod in the antenna is then calculated from the usual energy balance equation

$$mc\frac{dT}{dt}+\sigma\varepsilon A\,T^4 = \mathrm{ld}\,[\,\alpha_s \sin\beta(t)\,q_S + \alpha_e A_e(t)\,q_e] \tag{3.1-1}$$

where m is the mass of the rod, l is the length, d is the outer diameter, c is the specific heat, α_s and α_e are the absorbtivities for short and long wave respectively, σ is the Stefan-Boltzmann constant (5.67×10^{-8} $^{w}/_{m^2}$) and ε is the rod emissivity. The angle between the axis of the rod and the direction to the sun is β, which will be a function of time. A_e is a measure of the earth flux intercepted by the rod. Assuming that this flux is diffuse and isotropic at the top of the atmosphere, then at any altitude above the Earth the flux passing through an element of area is given by Cunningham.[30]

To provide an easy check of the numerically integrated results, values for the parameters above were selected to be similar to those of Mahaney.[31] Specifically, rod density was

Reproduced with permission of the copyright owner. Further reproduction prohibited without permission.

$1550\ ^{kg}/_{m^3}$, $\alpha_e = \alpha_s = 0.9$, $\varepsilon = 0.8$ and $c=1050\ ^{J}/_{kg\ K}$. The absorbtivity and emissivity correspond to uncoated graphite epoxy tube. Coating is not required in geosynchronous orbit because there is no atomic oxygen to degrade the composite. The numerical integration used a fourth-order, constant step size Runge-Kutta scheme. To eliminate transients, integration of equation 3.1-1 was performed around a complete orbit prior to using the numerical results . Figure 3.1-2 shows the temperature variation around the orbit for three selected rods in the antenna. By connecting grid points 23 and 31, rod 64 (see Appendix B) lies in the orbit plane and shows the largest solar effect. Rod 84, which connects 30 and 31, is nearly at right angles to the orbit plane and shows a minimal solar effect. Rod 235 connects grid 31 to the back structure and shows an intermediate effect.

The temperature deviations from the reference temperature 300^{o} K for all 420 rods are calculated throughout the orbit and the displacements of structural grid points are determined by using a sensitivity matrix calculated using NASTRAN. The sensitivity matrix provides the change in the z- location of the 61 reflecting surface grid points for a unit increase in length of each of the 420 rods. There are changes in the other two directions at each node; however, these have a small effect on the phase of the radio wave for shallow antennas, but could be included without difficulty if required. The sensitivity matrix will also be used for optimally locating actuators since the actuators will be assumed to provide a change in length of the rod to which it is attached. The displacements δz in the z-direction can be converted to phase changes using equation 2.1-8, $\Psi \approx (1+\cos\theta)\ \delta z$.

Radio Frequency Characteristics

The 55-meter antenna has an f-number of 1.5 and a focal length of 82.5 meters. An operating frequency of 30 GHz is assumed giving a wave length of 1 cm. It is also assumed that the feed is y- polarized so that $\vec{u}$ has the form given by 2.1-18, i.e.

Reproduced with permission of the copyright owner. Further reproduction prohibited without permission.

$$\vec{u} = \frac{-\cos\theta/2\,\{\sin\varphi\cos\varphi\,(1-\cos\theta)\,\vec{e_x} - (\sin^2\varphi\cos\theta + \cos^2\varphi)\vec{e_y}\} - \sin\varphi\cos\theta\sin\theta/2\,\vec{e_z}}{\sqrt{1-\sin^2\varphi\sin^2\theta}}.$$

High resolution radiometers will also have a highly tapered feed to increase beam efficiency. High beam efficiency implies suppressing the side lobes well below the diffraction limited value of -17 dB. A -30 dB level is used for the validation antenna as both a nominal design value and the goal for the control system to maintain. A cosine power law, as defined by Balanis[32] (page 624) is assumed for the taper:

$$G(\theta) = 2(n+1)\cos^n\theta, \quad 0 \le \theta \le \frac{\pi}{2} \text{ and } G(\theta) = 0 \text{ otherwise.}$$

A taper of 15 dB at the edge of the antenna, will provide a side lobe level of -30 dB, and this requires n = 62.

Thus $G(\theta,\varphi) = 126\cos^{62}\theta$. (3.1-2)

Figure 3.1-3 shows four sections through the far field pattern for a parabolic surface. The angles Θ and Φ are the far field point angle shown in figure 2.1-1. The $\Phi = 0$ and 60 curves coincide and the $\Phi = 30$ and 90 coincide. This is due to the selection of points on the surface to perform the integration, which results in the geometry being invariant under a 60 degree rotation. The difference between these two sets is due to the geometry not being invariant under an arbitary rotation. The difference could be reduced by selecting a smaller spacing for the numerical integration, but the 1 to 2 dB difference in the side lobes was considered accurate enough for this study.

The first term in the Zernike-Bessel expansion, $\vec{A}_{00}$ determines the far field at the center of the beam for an undistorted antenna. From 2.1-15,

Reproduced with permission of the copyright owner. Further reproduction prohibited without permission.

$$\vec{A}_{00} = \frac{1}{\pi}\int_0^{2\pi}\int_0^1 \vec{U}(\tau, \varphi)\,\tau\, d\tau\, d\varphi.$$

With these functions for $\vec{u}$(2.1-18) and G (3.1-2), the x and z components vanish and the y component becomes

$$A_{00_y} = \frac{\sqrt{126}}{\pi}\int_0^{2\pi}\int_0^1 \frac{\cos^{2}\theta/2\,\cos^{31}\theta(\sin^2\varphi\,\cos\theta+\cos^2\varphi)}{\sqrt{1-\sin^2\varphi\,\sin^2\theta}}\tau d\tau d\varphi$$

Based on a numerical quadrature, $A_{00_y} \approx 5.309$ (3.1-3)

Whenever, in subsequent discussions, the cost J_1 or J_2 (2.2-11 or 12) are given in dB, the reference will be $A^2_{00_y}$.

Reproduced with permission of the copyright owner. Further reproduction prohibited without permission.

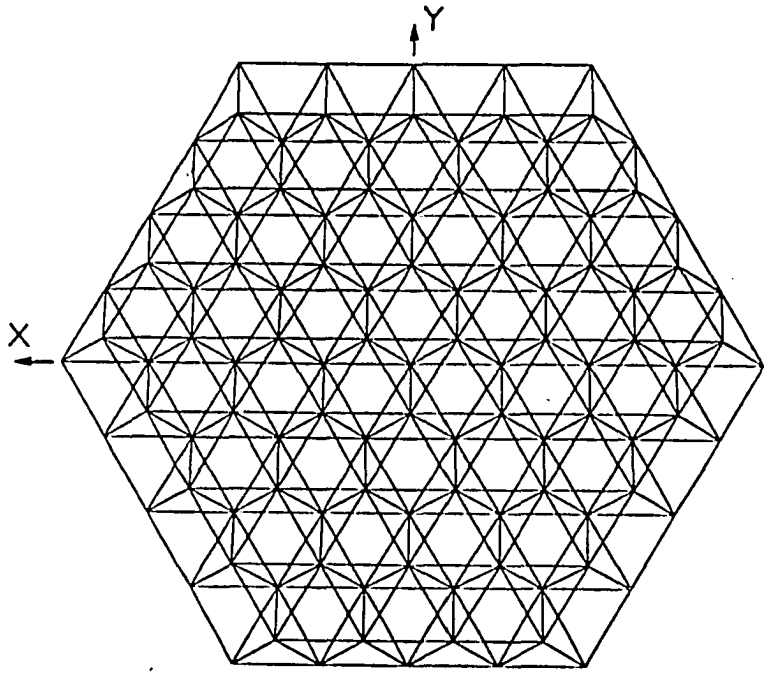

Figure 3.1-1. Geometry of the 55-meter tetrahedral truss.

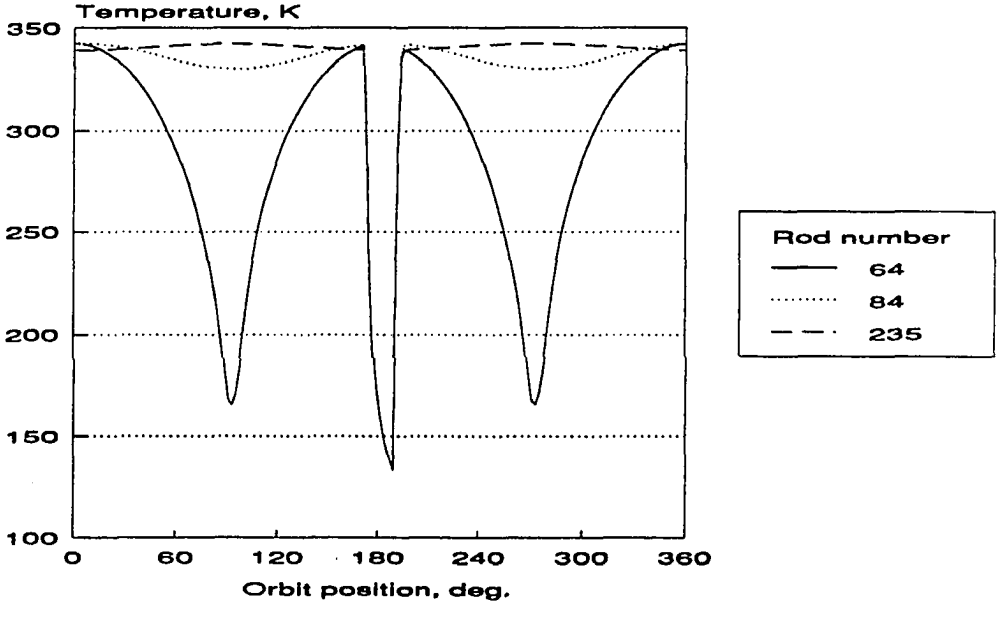

Figure 3.1-2. Temperature variations during one orbit for three typical rods.

Reproduced with permission of the copyright owner. Further reproduction prohibited without permission.

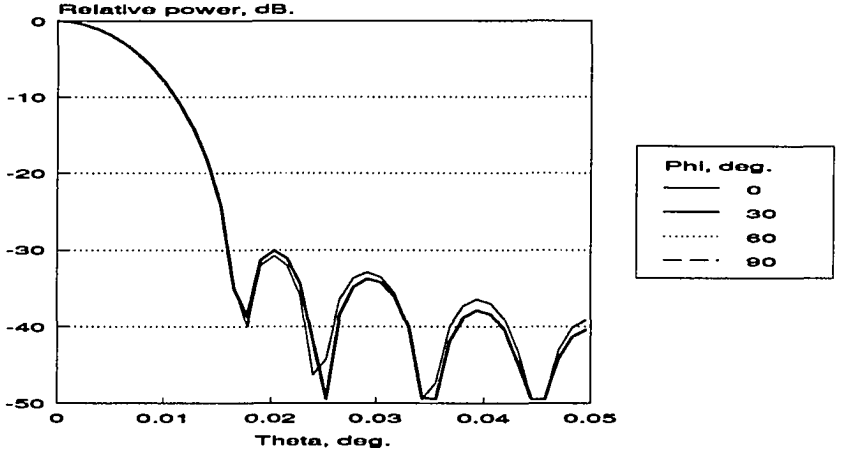

Figure 3.1-3. Far field pattern for 55-m parabolic reflector at 30 GHz with 15 dB. taper.

Reproduced with permission of the copyright owner. Further reproduction prohibited without permission.

3.2-Open Loop Control

This section will discuss the design and performance of an open loop control system, that is, a system where there is no feedback from sensors that measure the deviation from the desired state. Rather, it is assumed that there is perfect knowledge of the system and its enviroment. The next section will discuss the closed loop system and its performance.

A geosynchronous radiometer will experience a significant variation in the direction of solar flux during the 24 hour orbital period; and, for 22 days before and after the equinoxes, the satellite will pass through the shadow of the earth causing a rapid decrease in heating. The seasonal variations in solar heating are due to the apparent motion of the sun relative to the orbital plane. At the solstices, the sun will be either 23.5^{o} north or south of the orbital plane. This variation in declination of the sun causes the periodic heating due to the orbital motion to vary through the year. Since the satellite is fixed over one geographic area, the only variation in heat flux from the earth will be the diurnal/seasonal variations in emitted and reflected energy; however, the total flux from the earth is less than 6 $^{watts}/_{m^2}$ and even 20% to 30% variations[33] are going to be small compared to the solar flux variation taking place at the same time.

To design any control system it would be highly desirable to design for a single nominal condition and consider variations from that condition as robustness issues. For the geosynchronous case the nominal conditions will be equinox with the shadow of the earth neglected in calculating the solar heating input. The initial configuration has the earth and the sun at opposition as seen from the spacecraft. With these assumptions the design of the open loop system followed these main steps:

Reproduced with permission of the copyright owner. Further reproduction prohibited without permission.

1. Mapping Thermal Distortion into RF Parameters

The $G(t)$ matrices (2.2-4) were calculated at 180 equally spaced orbital positions using every second surface distortion result from the thermal analysis. During this process the value of J_1 can be determined (2.2-11) to identify the orbital position where the far field will be most distorted as measured by J_1. From figure 3.2-1 it is seen that double extrema in J_1 occur when the sun is illuminating the edge of the antenna. The maximum J_1 is about +3 dB and occurs at an orbit position of 114^o. The far field pattern corresponding to this position is shown in figure 3.2-2, where it can be seen that the thermal distortion has an unacceptable influence on the beam width when compared to figure 3.1-3. Note that, for 50% of the orbit, the value of J_1 exceeds -20 dB. It will be seen later that this is about the maximum value of J_1 that will meet the -30 side lobe goal.

2. Principal Component (PC) Analysis

The grammian H from equation 2.2-5 is approximated by arithmetically averaging the 180 GG^T matrices. The 20 largest eigenvalues of H and corresponding eigenvectors were extracted using a sub-space iteration method (Parlett, 1980, pg. 292, implementation #3), which converged to 6 places in the eigenvectors (sic) in less than 10 iterations. To confirm that all of the largest eigenvalues have been captured in the sub-space iteration, a value of J_2 using 2.2-12 was calculated from the eigenvalues and compared with the average value of J_1 from the first step. For the present case, 7 place agreement was obtained. The eigenvalue results are shown in figure 3.2-3. Only 4 PC's contribute more than -40 dB. The variation of the power, $g_i^T g_i$ from equation 2.2-7, for these PC's is shown in figure 3.2-4. Each PC is expected to contribute its maximum distortion to the far field at the time of maximum amplitude. Recall that the actuator strokes will be linear combinations of the PC amplitude functions $g_i(t)$. At the times of maximum amplitude,

Reproduced with permission of the copyright owner. Further reproduction prohibited without permission.

the far field distribution for each PC was determined and is shown in figure 3.2-5. The first three PC's, with maximum J_1 cost between +3 and -15 dB, must clearly be controlled, the fourth, with a maximum J_1 of - 19.9 dB, must be included if the side lobes are to kept below -30 dB, but the fifth and higher PC can be neglected if controlling the first four does not "excite" the higher PC's. From these results, a tenative criterion of -20 dB can be selected for the maximum value of J_1 that is acceptable. This criterion will need to be validated with further examples; but, if validated would mean that acceptable performance can be maintained as long as the distortion part of the far field contributes no more than 1% of the peak power.

3. Optimal Actuator Locations

Initially all 420 rods in the structure were considered as potential sites for length changing actuators. The sensitivity matrix generated in NASTRAN, as discussed in section 3.1, was mapped into 420 G_α matrices using equation 2.3-1. To perform the initial screening using 2.3-13 requires an assumption of the number, L, of PC's to be included in determining the effectiveness, ε_α. Step 2 above suggest that L must be 4 or greater. Selecting L to be 4 would assure the ability to control the nominal structural system and orbit geometry; but, may not provide a robust system that can accommodate off nominal conditions that no doubt will "excite" higher PC's. On the other hand picking L too large assures that higher PC's will be "excited" while controlling only the lower PC's. Two values of L (5 and 10) were selected for testing. Figure 3.2-6 shows the variation of ε_α with rod number when L=5 and table 3.2-1 summarizes the number of effective rods for four levels of ε_α. The 156 front surface rods generally have higher values (mean = 0.91) than the 120 back surface rods (mean = 0.86) and both are clearly more effective than the 144 rods that connect the front to the back (mean = 0.50). Figure 3.2-7 shows a similiar result when L=10. Over three times as many front surface rods have $\varepsilon_\alpha > 0.975$ than

Reproduced with permission of the copyright owner. Further reproduction prohibited without permission.

back surface rods. The relative ineffectiveness of the middle rods is due to the very localized surface distortions caused by middle rod extension; whereas, front and back rod extensions generally cause distortions with longer spatial wave lengths. The spatial wavelength of the PC generally decrease as the eigenvalue decreases. The front surface rods are clearly the most effective and no further consideration was given to back and middle rods unless the front rod set proved to be inadequate.

Having identified the effective locations for actuators, the next task is to find the optimal locations for some fixed number, M, of actuators. Given some initial configuration of actuators, the procedure to attach an actuator to the next most effective rod is given by equations 2.3-10 and 2.3-12. This process was tried for a case with L=10 and the condition that $\varepsilon_\alpha \geq 0.975$. The procedure started with the most effective rod, #31 connecting grid points 11 and 18 (see Appendix B for the rod connectivity table), then repeatedly added the next most effective rod. Before the number of rods, M, reached 5 it was found that this process added rods that had nearly proportional G_α matrices, leading to numerically unstable solutions. The $\varepsilon_{\alpha\beta}$ criteria, given by 2.3-14, was thus used as a second filter on the rods to be consider for actuator sites. Generally, the numerical solutions became unstable if two rods α and β were included in the set and $\varepsilon_{\alpha\beta} > 0.99$. With this criteria the procedure showed no tendency toward numerical instability. Thus a two step process was used to select candidate rods. Each rod must first pass the ε_α test. Then rods were compared pairwise to calculate $\varepsilon_{\alpha\beta}$. If $\varepsilon_{\alpha\beta}$ was too large the least effective of the two rods was dropped from the candidate set.

It became clear that only a few actuators were going to be required to control the thermal distortions and that the combinatorial explosion associated with the discrete optimization problem was not going to be serious. Thus, in an attempt to arrive at a more optimal set of actuators a 'two step forward-one step back' approach was used. In this approach

Reproduced with permission of the copyright owner. Further reproduction prohibited without permission.

equation 2.3-12 is used to sequentially add two actuator locations, then the actuator that has been in the selected set the longest is deleted. Each cycle of this process only adds one actuator. This procedure provided considerable confidence in the final results because it was found that after only a few cycles the deleted location was generally immediately returned to the set.

Ten sets of optimal locations were generated using two values of L (5 & 10) and 5 values of M (5,7,9,11 & 15). For both cases $\varepsilon_{\alpha\beta} < 0.98$ was used. For L=5, $\varepsilon > 0.95$ and for L=10, $\varepsilon > 0.975$ were used. The result are summarized in table 3.2-2. Rod 31 is the only rod that appears in every set; but, many rods, once added to the set, remain in the optimal set. Rods 75 and 76 have a $\varepsilon_{75,76} = 0.998$ and appear in 7 sets. They are an example of an effective pair that produce nearly proportional G_α matrices. The column labeled J_2 is the value obtained from equation 2.3-10 summed over the twenty PC's recovered from $\boldsymbol{H}$ as discussed in step 2. It will be seen later that this is not a reliable indicator of the actual value of J_2 that will result from the open loop control.

Each of the ten sets of actuator locations was used in conjunction with equation 2.3-4 to determine the optimal stroke variations $s_\alpha(t)$ throughout the orbit. The resulting Zernike-Bessel costs, calculated from

$$J_1 = \frac{2}{N} \|\delta \boldsymbol{G}\|^2 \equiv \frac{2}{N} \left| \left| \boldsymbol{G} - \sum_{\alpha=1}^{M} s_\alpha \boldsymbol{G}_\alpha \right| \right|^2,$$

are tabulated in table 3.2-3. Actuator strokes are shown for the case L = 5 and M = 5 in figure 3.2-8. The strokes are in the one millimeter neighborhood as assumed in section 3.1 during the discussion on buckling loads. It should be noted that the strokes reported here and elsewhere are equivalent unconstrained elongations. That is, the actuator forces are those necessary to extend an unconstrained rod the amount shown in figure 3.2-8.

Reproduced with permission of the copyright owner. Further reproduction prohibited without permission.

Actual elongations in the tetrahedral truss will be between 60% to 80% of the unconstrained values. Figure 3.2-9 shows the open loop variation of J_1 throughout the orbit for the limit cases in table 3.2-3. The figure demonstrates the expected trend that increasing the number of actuators reduces the Zernike-Bessel cost. But, another general result is also illustrated, namely, that the best performance is achieved with a given number, M, of actuators if the parameter L is selected to be about the same as M. The values of Zernike-Bessel average cost, J_2, shown in the table are the average J_1 over the orbit (2.2-12) and, when compared with the corresponding values in table 3.2-3, it is seen that the earlier predicted values do not agree well with the actual values. This must be due to the error introduced by truncating the cost (2.3-10) to 20 PC's since that is the only approximation in the process.

The largest value of J_1 for any of the case is -18.8 dB for the L = 5 and M = 5 case. At the orbit position corresponding to this J_1 the far field pattern was calculated, and is shown in figure 3.2-10. The peak power occurs at the desired center and is only 0.17 dB below the parabolic case shown in figure 3.1-3. The first side lobe is at -29.2 dB and is slighlty above the goal of -30 dB. It is to be noted from figure 3.2-9 that this violation will only occur during a small fraction of the orbit. Further, any of the other 9 cases from table 3.2-3 will provide acceptable far field patterns. This is a second case that suggest selecting - 20 dB for the maximum value of Zernike-Bessel cost, J_1.

Thus, as few as five actuators can control the far field pattern to acceptable levels for the nominal orbit. The next issue is the performance for off nominal cases. It should be noted from table 3.2-3 that for a -20 dB criterion, there is at most a 6 dB margin to handle the off nominal conditions with no more than 15 actuators.

Reproduced with permission of the copyright owner. Further reproduction prohibited without permission.

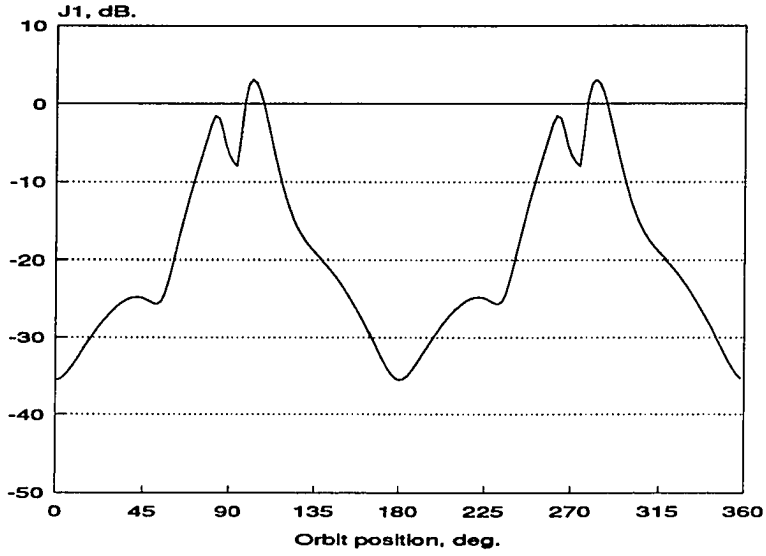

Figure 3.2-1. Zernike-Bessel cost, J_1, for the nominal case.

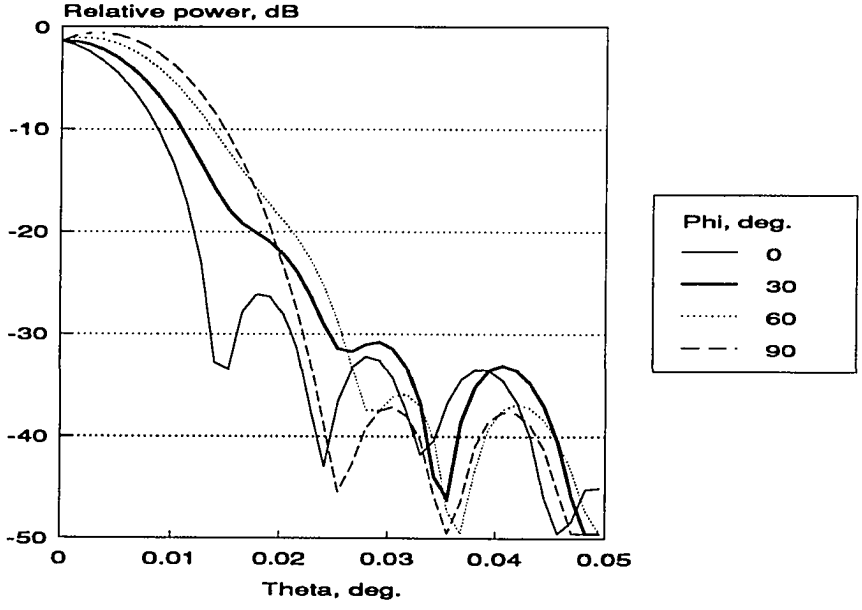

Figure 3.2-2. Far field pattern at maximum J_1. Orbit position = 114^o.

Reproduced with permission of the copyright owner. Further reproduction prohibited without permission.

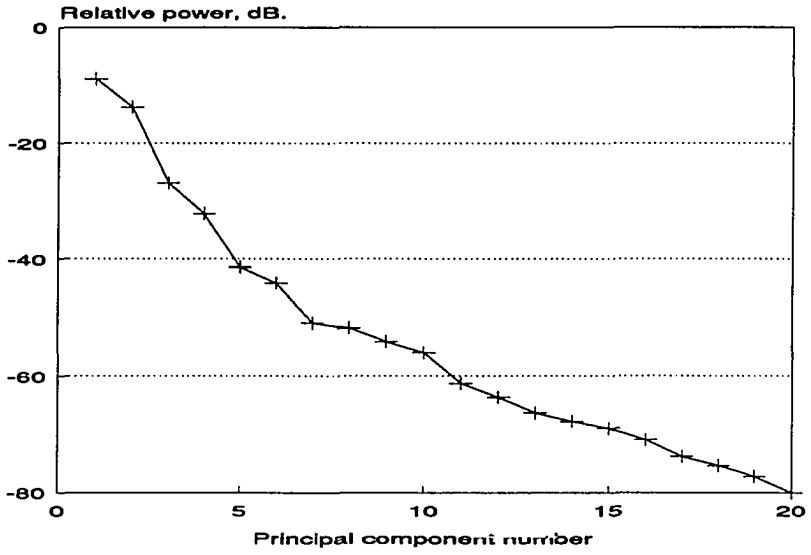

Figure 3.2-3. Twenty largest principal eigenvalues.

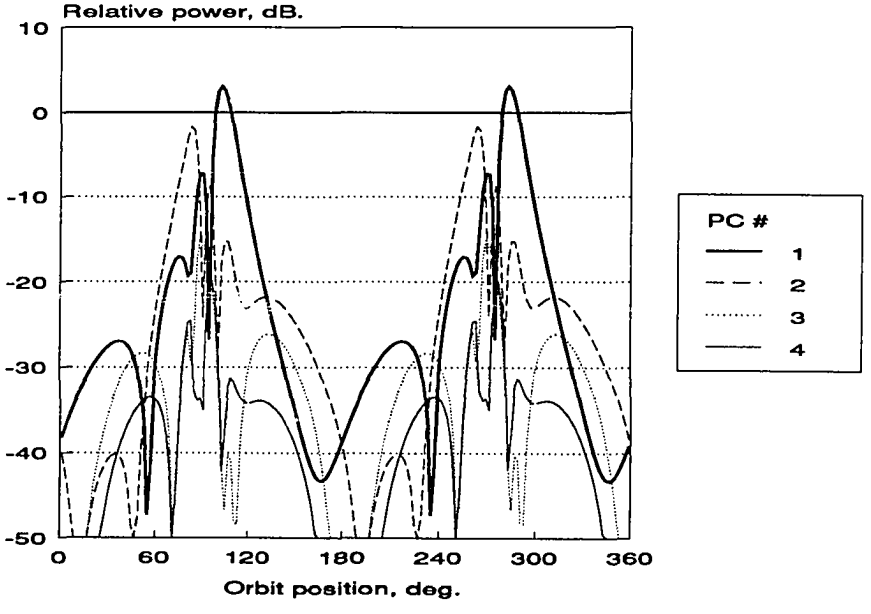

Figure 3.2-4. Power of the four largest principal components.

Reproduced with permission of the copyright owner. Further reproduction prohibited without permission.

Reproduced with permission of the copyright owner. Further reproduction prohibited without permission.

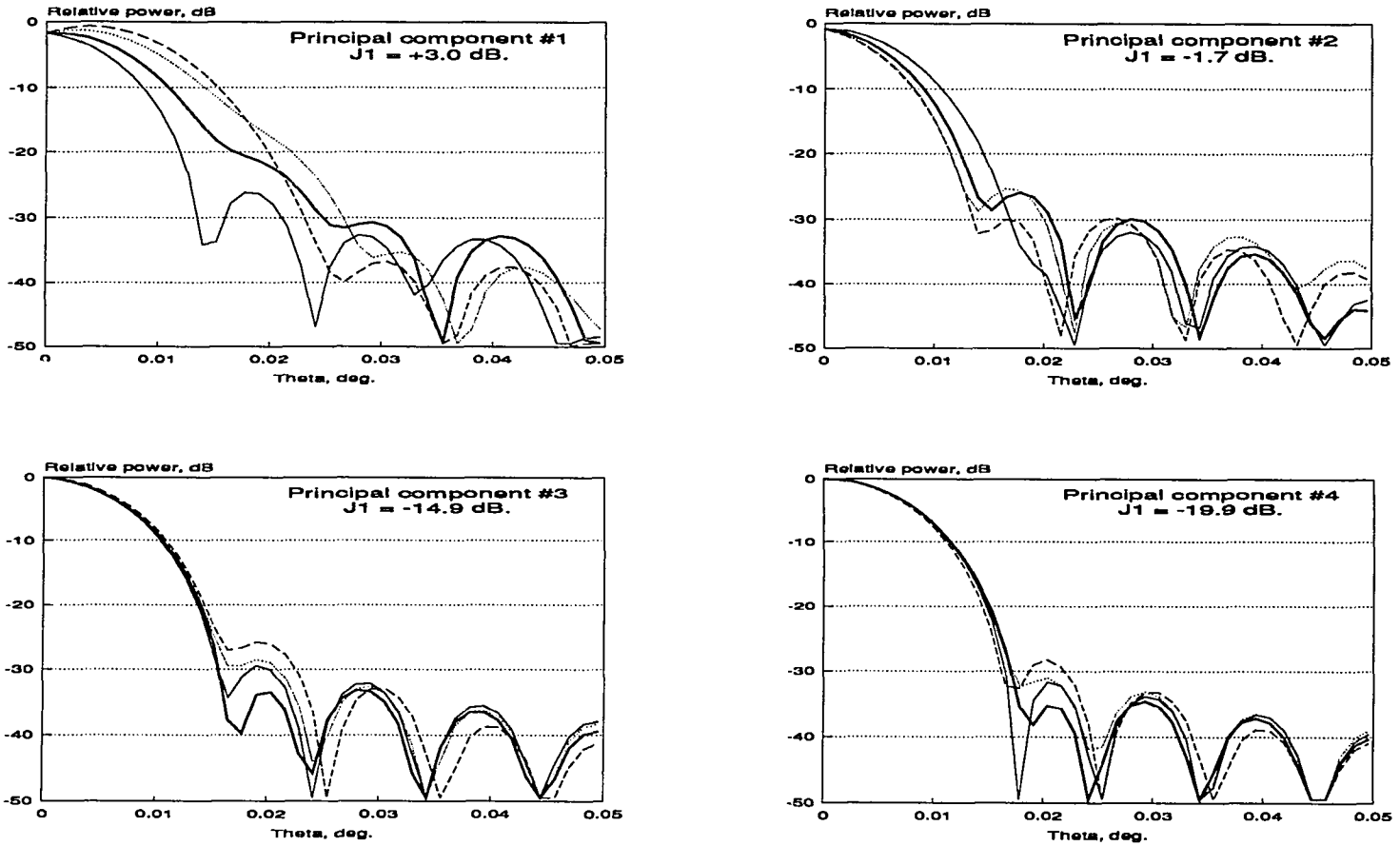

Figure 3.2-5. Far field corresponding to the four largest principal components at the times of respective maximum power.

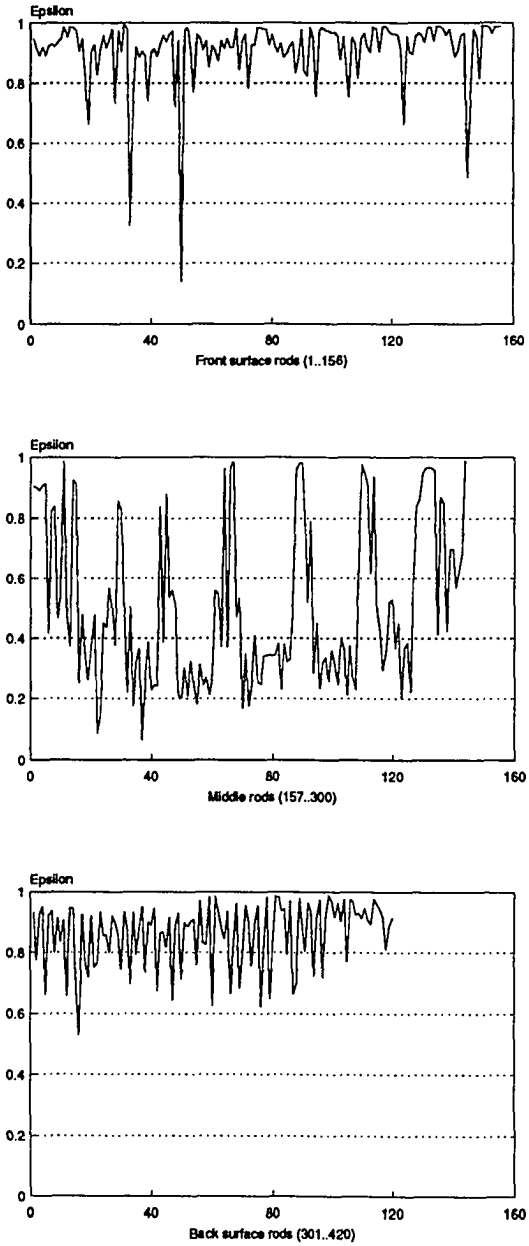

Figure 3.2-6. Rod effectiveness, ε_α, with L=5.

Reproduced with permission of the copyright owner. Further reproduction prohibited without permission.

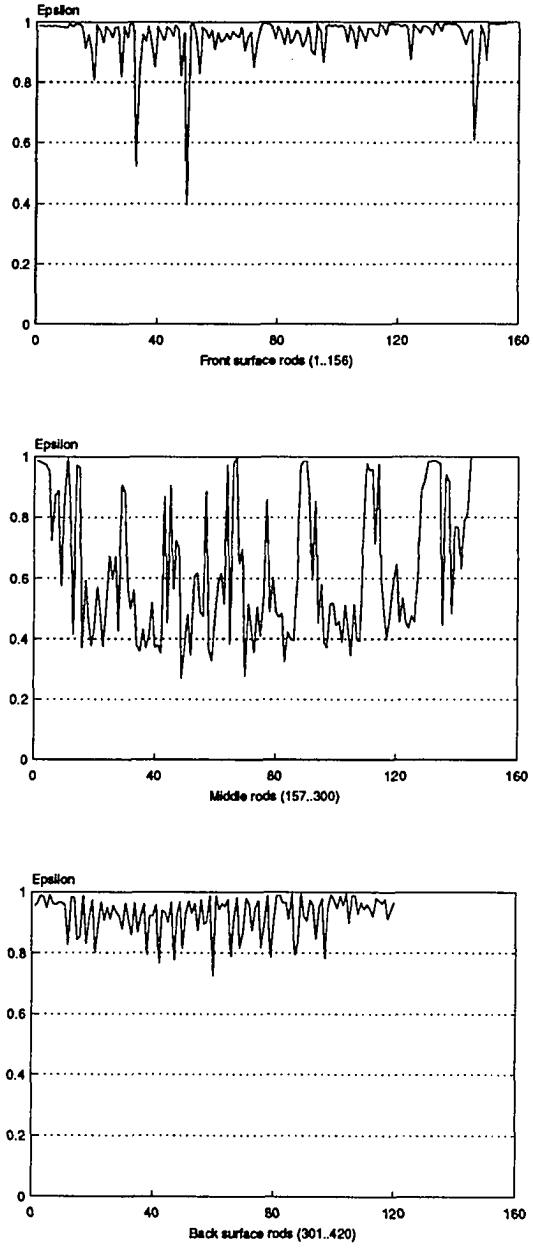

Figure 3.2-7. Rod effectiveness, ε_α, with L = 10.

Reproduced with permission of the copyright owner. Further reproduction prohibited without permission.

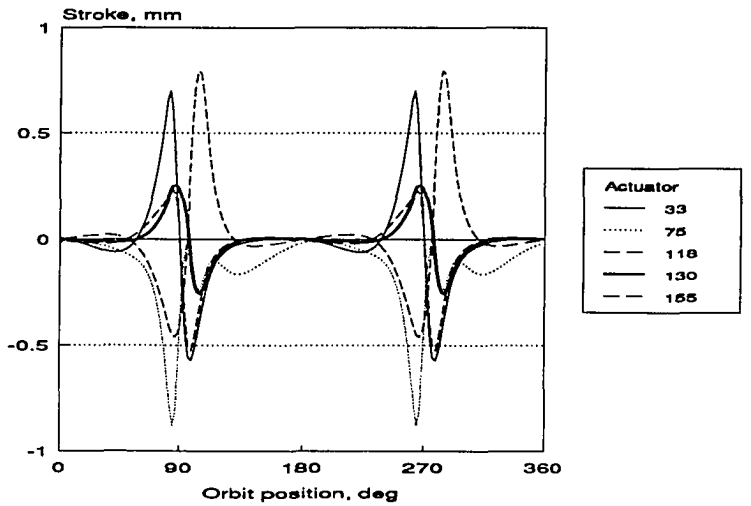

Figure 3.2-8. Actuator strokes for the nominal case with L = 5 and M = 5.

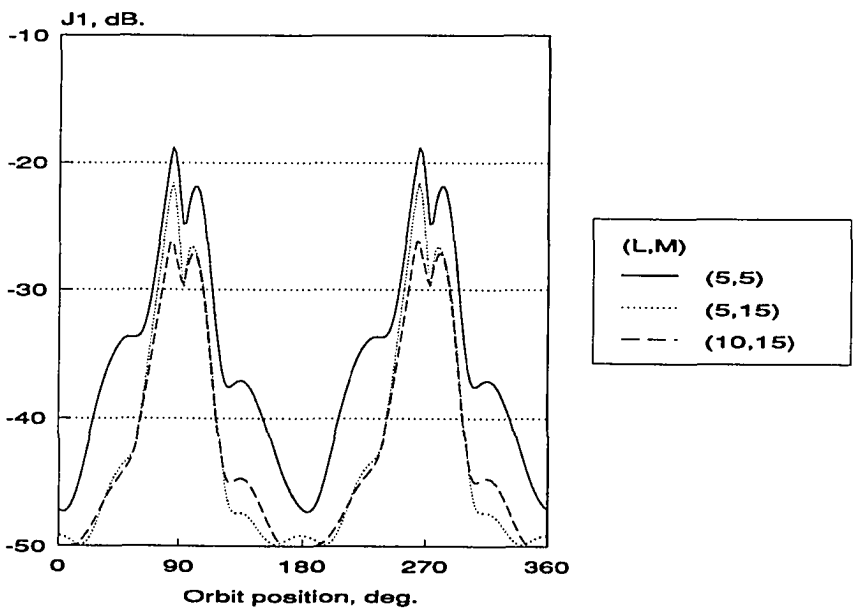

Figure 3.2-9. Effect of L and M on the nominal case cost.

Reproduced with permission of the copyright owner. Further reproduction prohibited without permission.

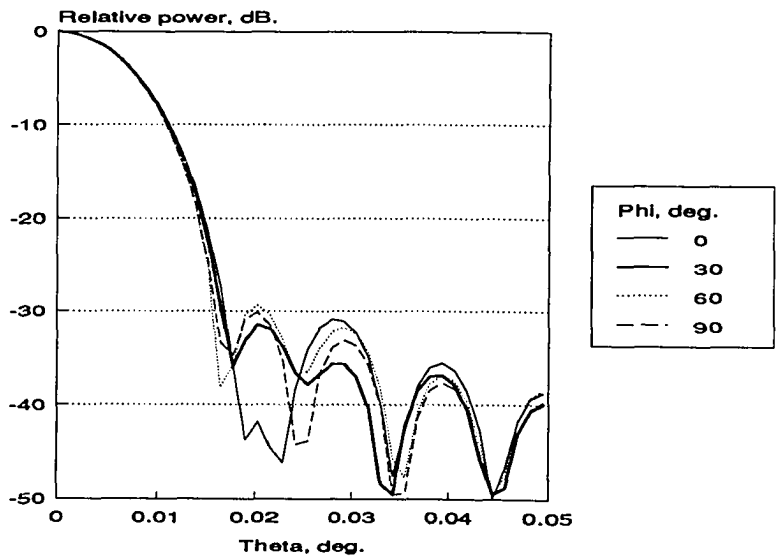

Figure 3.2-10. Far field at maximum J_1 with open loop control for L = M = 5.

Reproduced with permission of the copyright owner. Further reproduction prohibited without permission.

	L = 5			L = 10		
ε_α range	Front rods	Middle rods	Back rods	Front rods	Middle rods	Back rods
1.0-0.975	34	6	9	82	16	24
0.975-0.95	31	7	14	32	8	27
0.95-0.925	26	3	21	20	10	14
0.925-0.90	28	6	15	7	4	18
0.90-0.0	37	122	61	15	106	37
Mean ε_α	0.91	0.50	0.86	0.94	0.62	0.93

Table 3.2-1 Number of front, middle and back rods in specific ε_α ranges.

Reproduced with permission of the copyright owner. Further reproduction prohibited without permission.

Optimal actuator locations, L = 5, $\varepsilon\alpha_{min} = 0.95$, $\varepsilon\alpha\beta_{max} = 0.98$		
M	Rod number for actuator location	J_2,dB.
5	31, 75, 118, 130, 155	-29.8
7	31, 44, 75, 78, 118, 130, 155	-32.3
9	31, 34, 75, 78, 118, 125, 130, 139, 155	-34.3
11	31, 44, 46, 78, 102, 111, 118, 125, 130, 139, 155	-37.1
15	31, 44, 46, 47, 75, 78, 100, 102, 111, 118, 125, 129, 130, 144, 155	-40.2

Optimal actuator locations, L = 10, $\varepsilon\alpha_{min} = 0.975$, $\varepsilon\alpha\beta_{max} = 0.98$		
M	Rod number for actuator location	J_2,dB.
5	31, 76, 100, 126, 150	-29.8
7	2, 31, 43, 76, 100, 126, 150	-32.9
9	2, 31, 43, 76, 98, 100, 118, 126, 150	-36.0
11	2, 20, 31, 43, 76, 98, 118, 126, 139, 150, 154	-38.6
15	2, 20, 31, 43, 46, 76, 83, 98, 107, 111, 118, 126, 139, 150, 155	-41.1

Table 3.2-2 Results of optimal actuator location study.

Reproduced with permission of the copyright owner. Further reproduction prohibited without permission.

L = 5			
M, # actuators	Max. stroke, mm.	Max. J_1, dB.	J_2, dB.
5	0.90	-18.8	-28.4
7	0.80	-20.5	-29.9
9	0.75	-20.7	-30.7
11	0.74	-20.9	-30.9
15	0.73	-21.6	-32.4

L =10			
M, # actuators	Max. stroke, mm.	Max. J_1, dB.	J_2, dB.
5	1.2	-19.0	-27.8
7	1.2	-21.2	-29.4
9	0.9	-22.1	-31.1
11	0.8	-24.9	-33.0
15	0.64	-26.2	-34.5

Table 3.2-3 Results of open loop control for nominal case.

Reproduced with permission of the copyright owner. Further reproduction prohibited without permission.

3.3-Robustness of Nominal System

The optimal actuator locations developed in section 3.2 were based on a nominal orbital heating condition and assumed perfect knowledge of the structural and thermal properties of the antenna. The issue of the effectiveness the open loop system for off nominal conditions will be addressed in this section.

Other Orbit Configurations.

The nominal orbit ignored the shadow of the earth, which as seen in figure 3.1-2 has a dramatic effect on rod temperature. While in the shadow, however, all rods are at about the same temperature, so the deviation for a parabolic shape could be small. To quantify the effect on the far field pattern the shadow was included in the thermal calculations and the $G(t)$ matrices of equation 2.2-4 were regenerated. The maximum J_1 of +3.09 dB was the same as the nominal case while the J_2 value was 0.6 dB higher. Equation 2.3-4 was used to determine the optimal actuator strokes. The resulting open loop variation in J_1 is shown in figure 3.3-1 for the actuator locations corresponding to the case of L = 5 and M = 5 in table 3.2-2 and can be compared to the nominal case in figure 3.2-9. Before the satellite goes into shadow the results are the same as the nominal case and within 15 minutes after exiting from the shadow the results are essentially the same. During the shadow period the value of J_1 peaks 5 dB below the maximum of -18.8 dB, which is, of course, the same as the nominal case. Thus, the transients produced by the shadow of the earth produce no more difficulty than the nominal case.

The nominal case also assumed an equinox position for the sun; that is, the sun is in the plane of the orbit. At solstices the sun is 23.5^0 north or south of the orbit plane. Again $G(t)$ matrices were regenerated for both solar locations and the open loop control was applied. With the sun at maximum northerly (southerly) declination a maximum J_1 of

Reproduced with permission of the copyright owner. Further reproduction prohibited without permission.

+5.03 (+4.94) dB. occured during an orbit. These are about 2 dB higher than the nominal case and will require more actuators to meet the -30 dB maximum side lobe goal. With less than 11 actuators the J_1 value is greater than -20 dB; but, the case with L = 5 and M = 11 is at -19 dB. So detailed RF calculations will be required to validate this case. Figure 3.3-2 shows the open loop control value of J_1 for this case (L = 5 and M = 11) and figure 3.3-3 gives the far field at the maximum J_1. The first side lobe is at -29.4 dB, thus, there will only be short periods when the open loop system with 11 actuators can not meet the -30 dB side lobe requirement. Fewer actuators give longer violation of the side lobe goal.

System Errors.

Another possible limitation of the open loop system is the accuracy of the structural model. Individual elements of the structure will vary in cross section measurements, in elastic modulus, in coefficient of thermal expansion, emissivity, absorbtivity, etc. In order to begin to quantify some of these effects a number of simulations were performed. In the first simulation the 420 rods in the structure were assumed to have errors in EA that are uniformly distributed between ±2%. Such errors are consistent with manufacturing tolerances for large graphite epoxy tubes (H. Bush, private communication). These errors have two effects on the results. First, the distortions due to thermal effects will be different than the nominal case, and second, the sensitivity of the surface changes due to actuator forces will be different.

In this simulation one random sample was generated for the EA of the 420 rods. A new sensitivity matrix was generated in NASTRAN that was used to calculate the thermal distortion throughout the orbit. The actuator strokes were calculated using the sensitivity matrix without errors; but, when these strokes were used to calculate the surface corrections, the erronous sensitivity matrix was used.

Reproduced with permission of the copyright owner. Further reproduction prohibited without permission.

The maximum value of the uncontrolled cost J_1 was within 0.1 dB of the nominal maximum cost, suggesting that manufacturing errors at this level would be acceptable from the radiometer performance standpoint. Further, the maximum value of the controlled cost was within 0.4 dB of the nominal maximum controlled cost for L = 5 and M = 5 or 11. Although there is a degradation of controlled performance it is probably not severe enough to justify increased quality control for the rods.

The final system errors considered are errors in the thermal properties of the structure, namely the coefficient of thermal expansion, the emissivity and the absorbtivity. These parameters directly determine the temperature of the rods and/or directly influence the surface distortion. The error in CTE due to the manufacturing process would be due to the same type of errors that produce variations in EA; thus, a 2% uniform distribution is assumed for CTE. Optical properties for coating can vary greatly during the manufacturing process and can change with age in orbit. However, the rods for this study are uncoated graphite epoxy and nearly black. Thus only small variations in α and ε are expected. Again a uniform distribution of 2% is selected. The maximum uncontrolled value of J_1 was 0.1 dB. lower than the nominal case and the uncontrolled value of J_2 was 0.2 dB higher. After applying the open loop control with five actuators the maximum value of J_1 was reduced to -18.5 db, similiar to the nominal case; however, the variation of cost throughout the orbit is significantly different as seen in figure 3.3-5. Whereas for the nominal case, and the other variation from the nominal presented above, the cost decreased significantly away from the peak, this is not true for this case. The reason for this behavior is that 2% variations in the emissivity and absorptivity produce variations in temperature that can be as large as 5^{o} K. This may not seem large; but, for the nominal case at an orbit position of zero, the maximum temperature excursion across the entire antenna is only 26^{o} K. These errors thus introduce a random component with a significant amplitude which introduces a significant random variation in the aperture phase. These

Reproduced with permission of the copyright owner. Further reproduction prohibited without permission.

random variations produce a background in J_1 of about -24 dB. that cannot be corrected by the open loop system. Increasing the number of actuators to 15 reduces the peak to -21.86 dB, but there is still the high background around -25 dB. Figure 3.3-6 gives the far field at the maximum cost. As expected, with J_1 = -18.5 dB, the side lobes do not meet the -30 dB goal and the beam width is broadened noticably. The case with 15 actuators provides marginally acceptable far field performance.

Reproduced with permission of the copyright owner. Further reproduction prohibited without permission.

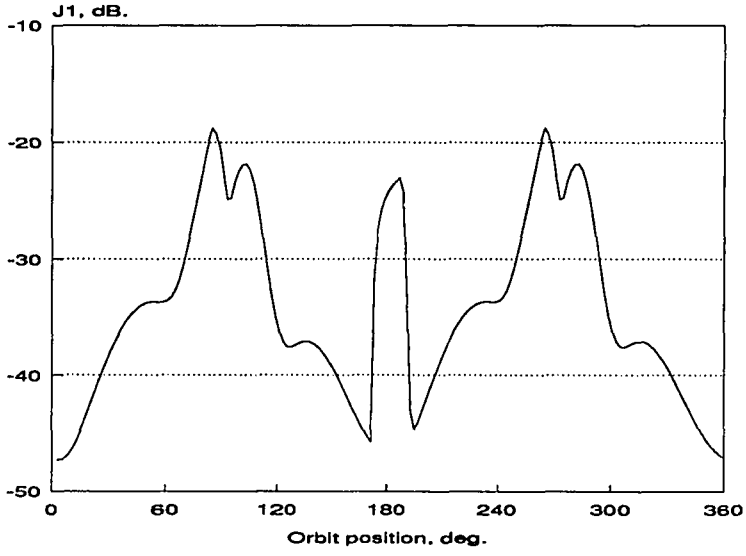

Figure 3.3-1. Open loop cost, J_1, with the earth shadow included.

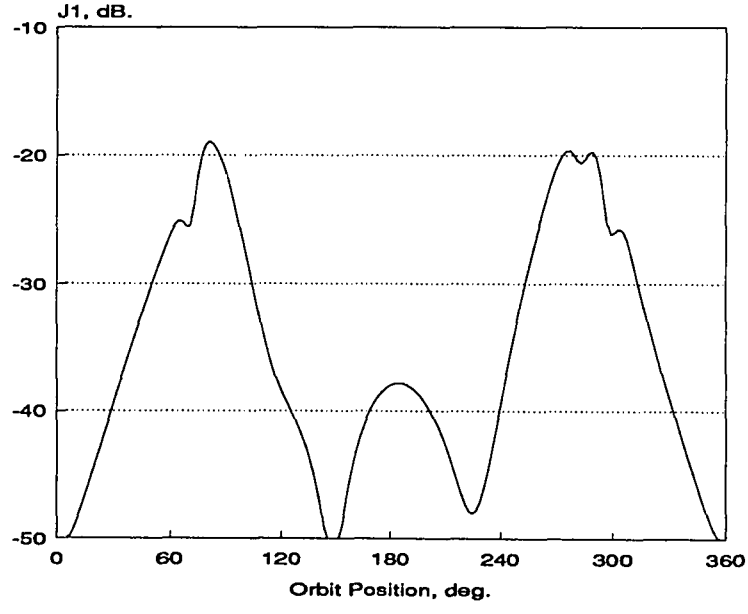

Figure 3.3-2. Open loop cost, J_1, with the Sun at 23.5^{o} north declination.

Reproduced with permission of the copyright owner. Further reproduction prohibited without permission.

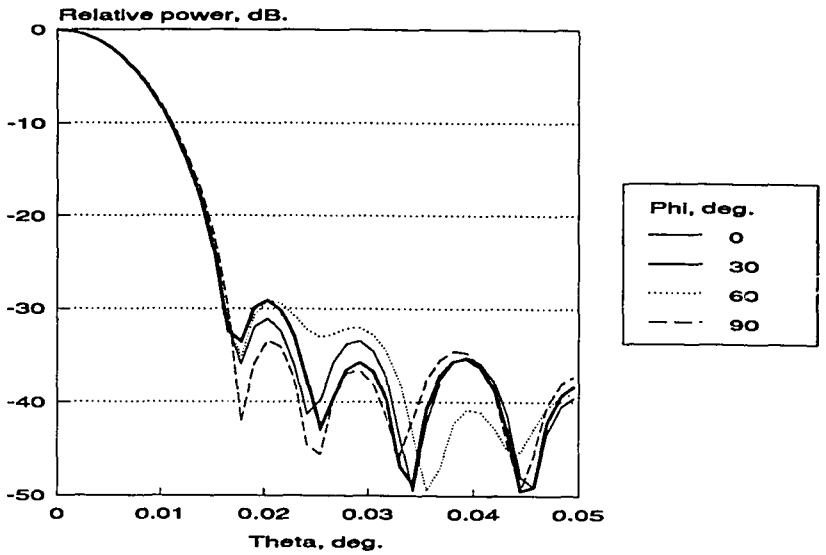

Figure 3.3-3. Open loop far field pattern with the Sun at 23.5^0 north declination

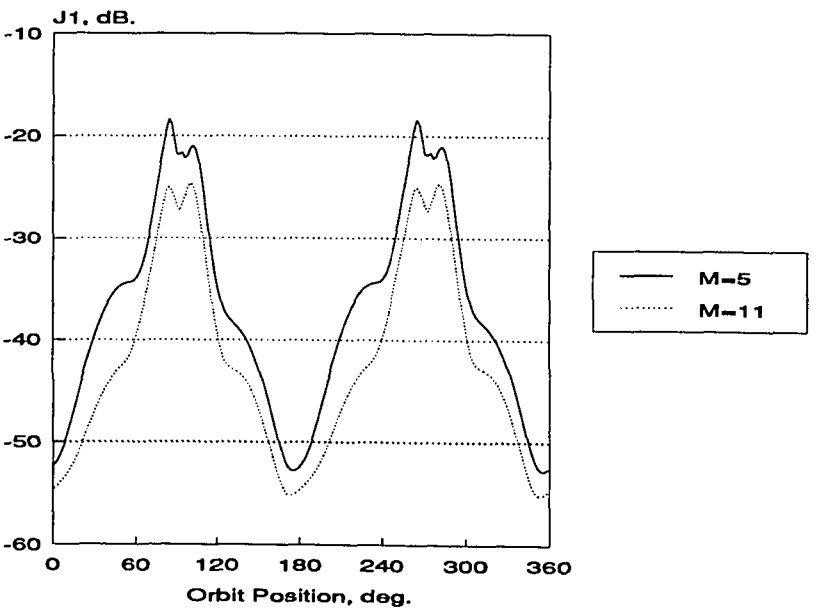

Figure 3.3-4. Open loop cost, J_1, with 2% random error in EA.

Reproduced with permission of the copyright owner. Further reproduction prohibited without permission.

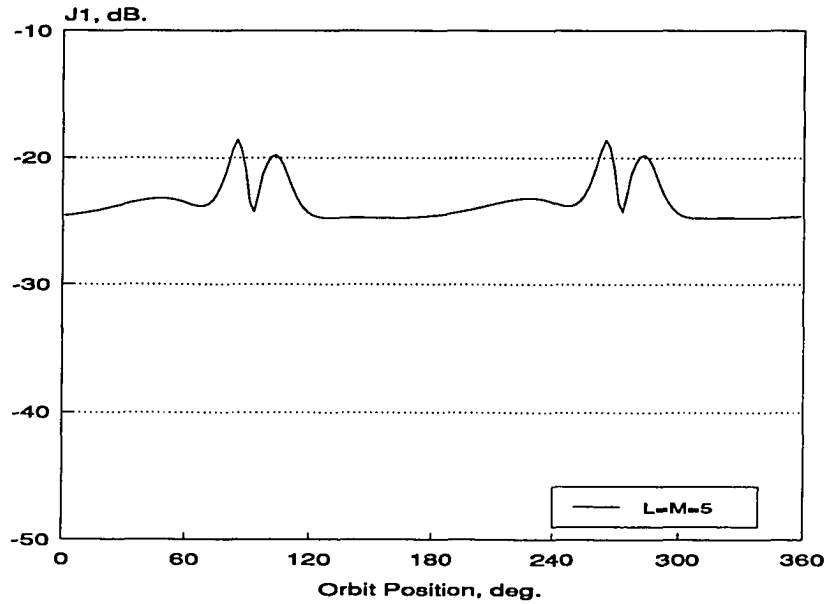

Figure 3.3-5. Open loop cost with 2% errors in CTE, absorptivity and emissivity.

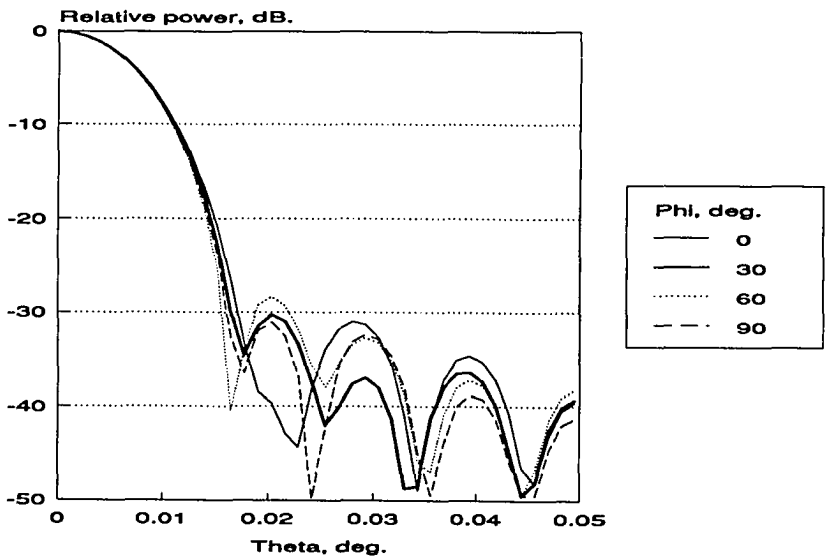

Figure 3.3-6. Open loop far field with 2% errors in CTE, absorptivity and emissivity.

Reproduced with permission of the copyright owner. Further reproduction prohibited without permission.

3.4-Closed Loop Control

As discussed in section 2.4, the closed loop system will utilize measurements of surface deviations to estimate one column of the G matrix using equations 2.4-3 and 2.4-4, from which the full $\hat{G}$ matrix can be formed. Then the actuator strokes will be calculated from equation 2.3-4 with $\hat{G}$ replacing G on the right hand side. The first question is where to place the sensors. For the validation antenna the illumination of the surface is nearly independent of the angle φ because of the assumed y-polarization and the feed gain function (3.1-2), so it is natural to select sensor locations that are uniformly distributed in φ. In addition, because of the high taper, it is more important to measure the distorted shape near the center than at the edges. Based on these arguments, two arrays of sensors were assumed as shown in figure 3.4-1. Thirteen sensors are denoted by circles at the nodes to which the sensor is assumed to be attached. In the second case, an additional 6 sensors, denoted by the squares, are on the perimeter to give a total of nineteen. These two cases will be denoted by S=13 and S=19 respectively. The second question is how many principal component amplitudes to estimate using equation 2.4-3. Two values were selected for this study, P=5 and P=10.

All of the simulations reported in section 3.3 on open loop robustness were performed as closed loop simulations. For the nominal case, the case with 2% variation in EA and for the case with the earth shadow, the values of J_1 were within less than 1 dB of the open loop results for any of the combinations of P and S above. Thus for these cases, estimating only five principal component magnitudes from as few as thirteen sensors yields essentially the same performance as assuming perfect knowledge of the system. For the case of the Sun at maximum declination; however, estimating five components was not adequate. This can be seen by comparing the open loop case with the closed loop case shown in figures 3.3-2 and 3.4-2 respectively. Both case have 11 actuators located at the

Reproduced with permission of the copyright owner. Further reproduction prohibited without permission.

positions in the top of table 3.2-2. Estimating only five components (P=5) results in a value of J_1 of -14.1 dB, which would not meet the goal. It should be noted however that the -20 dB limit is exceeded for only a small part of the orbit. Increasing the number of estimated components to 10 provides what appears to be acceptable closed loop performance. Further increasing the number of sensors to 19 does not provide any additional improvement. With P=10 and S=13, the far field at the maximum cost (figure 3.4-3) has side lobes below the -30 goal; however, it is noted that the second side lobe is also at -30 dB. This suggests further study of the far field pattern. Figure 3.4-4 shows additional sections through the pattern. It is seen that in the third quadrant, the -30 dB goal is not reached. Thus it appears that to reach the -30 dB goal will require more than 13 sensors; but a closed loop system with 13 sensors, estimating 10 principal component magnitudes would be adequate to control this case for all but a short time during the orbit.

Finally, the case with 2% errors in CTE, absorptivity and emissivity was simulated with the closed loop system with P=5 and S=13 for both 5 and 15 actuators. The closed loop system provided a better value for the maximum J_1 in both cases than the open loop system. For M=5(15) it was 0.2(0.8) dB better. Thus, as expected, the closed loop system performs better than perfect knowledge in the presence of system errors. The far field pattern, figure 3.4-5, also shows a modest improvement over the open loop pattern in figure 3.3-6.

Reproduced with permission of the copyright owner. Further reproduction prohibited without permission.

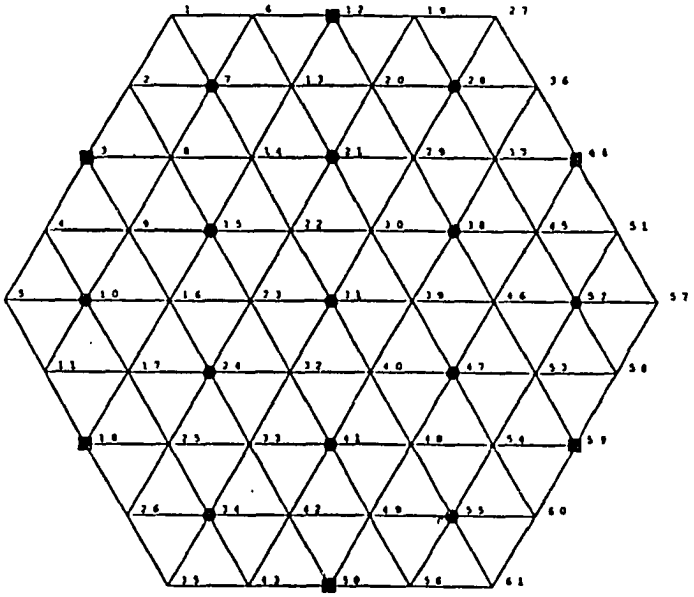

Figure 3.4-1. Sensor locations on the front surface .

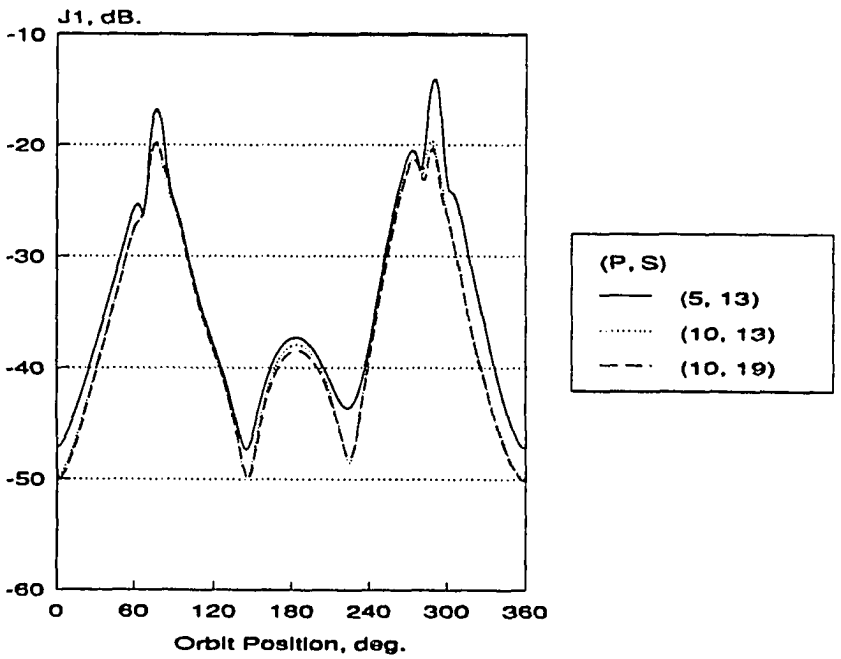

Figure 3.4-2. Closed loop cost, J_1, with the Sun at 23.5^0 north declination.

Reproduced with permission of the copyright owner. Further reproduction prohibited without permission.

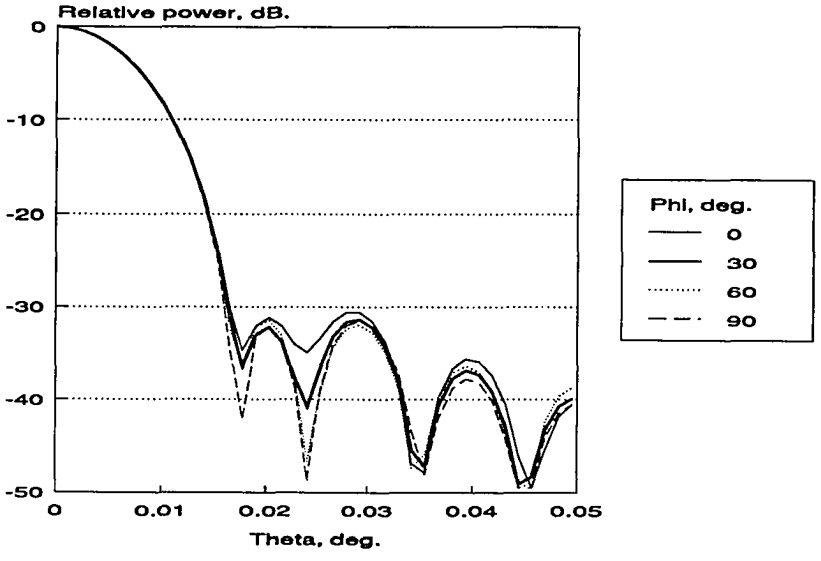

Figure 3.4-3. Closed loop pattern, Sun at 23.5^{0} north declination, first quadrant.

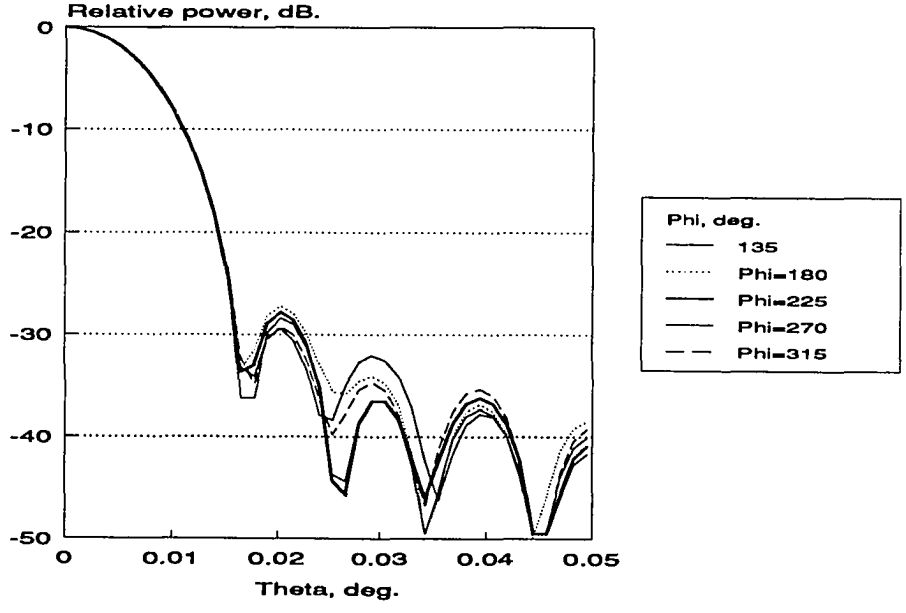

Figure 3.4-4. Closed loop pattern, Sun at 23.5 ^{0} north declination, other quadrants.

Reproduced with permission of the copyright owner. Further reproduction prohibited without permission.

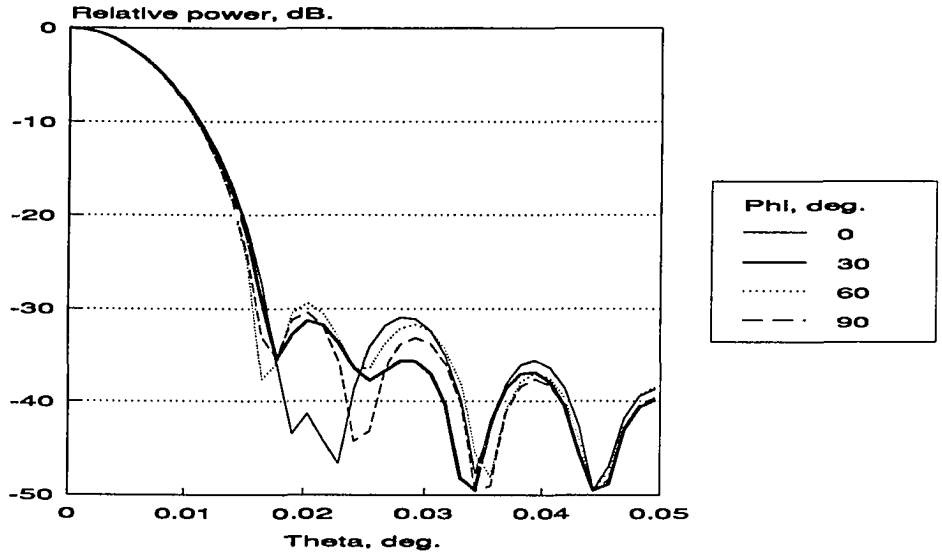

Figure 3.4-5. Closed loop pattern for 2% errors in CTE, absorptivity and emissivity.

Reproduced with permission of the copyright owner. Further reproduction prohibited without permission.

Chapter 4-Concluding Remarks

A theoretical basis has been developed for controlling the thermal distortions of large space radiometers due to orbital motion. The original objective of developing a control system cost function that is quadratic in form and is directly related to radiometer performance has been met by expanding the far zone electric field in a Zernike-Bessel series. In this expansion the cost function naturally appears and it is shown that this cost is a consistent indicator of the deviation of the far field from the desired pattern. The second of the original objectives, to include the temporal variations in the development of the optimal actuator locations, was accomplished by expanding an aperture integral using a principal component analysis. It is shown that the eigenvalues are directly related to average deviations of the far field pattern from the desired pattern. Further, the eigenvectors are used as a basis for directly estimating far field deviations from sensors measurements.

Simulations for a geosynchronous radiometer demonstrate that the method provides a convenient and meaningful means to quantify the influence of various orbit geometries and deviations of the system from nominal due to manufacturing and other errors.

The simulations also suggest that for the particular antenna geometry studied, 5 actuators and 13 sensors are adequate to control the nominal case and some deviations from nominal; but, that 11 actuators and 19 sensors are required to control the worst case studied.

Reproduced with permission of the copyright owner. Further reproduction prohibited without permission.

Although the process may appear to be computationally intensive, except for two NASTRAN static analyses, all of the calculations were performed on a 16 MHz 80386/80387 computer, usually in 64 bit arithmetic. Some typical times for calculations include 12 minutes to calculate the temperatures of 420 rods at 360 orbital postions integrating equation 3.1-1 and then mapping the temperature variations into reflecting surface deviations, 13 seconds to calculate $G(t)$ matrices at 180 orbit positions using equation 2.2-4 and forming the grammian (2.2-5), two minutes to extract 20 eigenvectors and eigenvalues of the grammian, 30 seconds to calculate 420 G_α matrices of equation 2.3-1, 15 minutes to determine the optimal locations for 15 actuators using the method described in section 3.1, and finally less than 3 minutes to calculate optimal actuator strokes at 180 orbital positions using equation 2.3-4 for either the open or closed loop simulations.

Like most research projects there remain a number of unexplored areas and open questions. A few of these are mentioned here.

1. The Zernike-Bessel cost, which reliably predicted performance for the 55 meter antenna, should be validated for other feed polarizations and gain functions and other antenna geometries, such as offset feeds to clear the aperture and off center feeds for scanning.

2. Low earth orbit (LEO) geometries should also be explored. Sun synchronous low orbits will be somewhat similiar to the geosynchronous case, since the sun will appear to move from one side of the orbit plane to the other through a limited angle during the year. Other orbits will be more challenging since there are large variations in the direction to the sun in just a few weeks due to orbital precession. Temperature variations are moderated by the radiation from the earth and the required coatings in LEO. On the other hand, the control system must accommodate the geographic, seasonal and diurnal variations in the flux from the earth.

Reproduced with permission of the copyright owner. Further reproduction prohibited without permission.

3. The Zernike-Bessel cost approach may also be useful for determining the significance of forced or free vibration modes on antenna performance.

4. The principal component analysis can be directly applied to obtain representations of distortions of spacecraft with other geometrical shapes, for example, long straight booms or flat platforms.

Reproduced with permission of the copyright owner. Further reproduction prohibited without permission.

References

[1]Ride, Sally K.,"Leadership and America's Future in Space," NASA Publication, August 1987.

[2]Litman, V. & J. Nicholas, "Guidelines for Spaceborne Microwave Remote Sensors," NASA Reference Publication 1086, 1982.

[3]Keafer, L.S. Jr., & R.F. Harrington, "Radiometer Requirements for Earth-Observation Systems Using Large Space Antennas," NASA RP 1101, 1983.

[4]Hedgepeth, J.M., "Critical Requirements for the Design of Large Space Structures," NASA Contractor Report 3484, 1981.

[5]Sharp, G.R., L.D. Gilger & K.E. Ard, "Extreme Precision Antenna Reflector Study Results," NASA Conference Publication 2368, Part 1, pp. 279-300, 1985.

[6]Tompkins, S.S.,"Effects of Thermal Cycling on Composite Materials for Space Structures," NASA Conference Publication 3035, Part 2, pp. 447-470, 1988.

[7]Tompkins, S.S., D.E. Bowles, J.G. Funk, J.A. Lavoie, T.W. Towell, "Development of Composite Materials for Spacecraft Precision Reflector Panels," Vugraphs from Composite Materials for Optical and Electro-Optical Instruments, Orlando, Florida, April 1990.

[8]Hardy, J.H., "Active Optics-Don't Build a Telescope Without It!," Procedings of International Conference on Advanced Technology Optical Telescopes, SPIE, Vol. 332, March 1982, pp. 252-259.

[9]Haftka, R.T. & H.M. Adelman, "An Analytic Investigation of Shape Control of Large Space Structures by Applied Temperature," AIAA Journal, Vol. 23, March 1985, pp. 450-457.

[10]Haftka, R.T. & H.M. Adelman, "Selection of Actuator Locations for Static Shape Control of Large Space Structures by Heuristic Integer Programing," Control and Structures, Vol. 20, No. 1-3, pp. 575-582, 1985b.

[11]Padula, S.L., H.M. Adelman, M.C. Bailey, & R.T. Haftka, "Integrated Structural Electromagnetic Shape Control of Large Space Antenna Reflectors," AIAA Journal, Vol. 27, No. 6, June 1989, pp. 814-819.

[12]Collin, R.E., & F.J. Zucker, "Antenna Theory," McGraw- Hill Book Co., Parts 1 and 2, 1969.

Reproduced with permission of the copyright owner. Further reproduction prohibited without permission.

[13]Acosta, R.J., "Generalized Single Reflector Analysis Program," NASA Lewis Research Center, Informal Report, December, 1988.

[14]Born, Max, & E. Wolf, "Principles of Optics," Pergamon Press, 1987.

[15]Ruze, J., "Antenna Tolerance Theory-A Review," Proceedings of the IEEE, Vol. 54, No. 4, April 1966, pp. 633-640.

[16]Stutzman, W.L. & G.A. Thiele, "Antenna Theory and Design," John Wiley & Sons, New York, 1981.

[17]Pearson, K., "On Lines and Planes of Closest Fit to Systems of Points in Space," Phil. Mag., Vol. 2, 1901, pp. 559.

[18]Hotelling, H., "Analysis of a Complex of Statistical Variables into Principal-Components," J. Educ. Psych., Vol. 24, 1933, pp. 417-441, 498-520.

[19]Eckart, C. & G. Young, " A Principal Axis Transformation for Non-hermitian matrices," Bull. Am. Math. Soc., Vol. 45, 1939, pp. 118.

[20]Lorenz, E.N., "Empirical Orthogonal Functions and Statistical Weather Prediction," Scientific Report No. 1, 1956, Stat. Forec. Proj., Mass. Inst. Tech., Cambridge, MA.

[21]Preisendorfer, Rudolph W., F.W. Zwiers, & T.P. Barnett, "Foundations of Principal Component Selection Rules," SIO Reference Series 81-4, Scripps Institution of Oceanography, Univ. of Calif, 1981.

[22]Moore, Bruce C., "Principal Component Analysis in Linear Systems: "Controllability, Observability, and Model Reduction," IEEE Transactions on Automatic Control, Vol. AC-26, No. 1, 1981, pp. 17-32.

[23]Kubrusly, C.S. & H. Malebranche, "Sensors and Controllers Locations in Distibuted Systems-A Survey," Automatica, Vol. 21, No. 2, pp 117-128, 1985.

[24]Skelton, R.E., and M.L. DeLorenzo, "Selection of Noisy Actuator and Sensors in Linear Stochastic Systems," J. of Large Scale Systems, Theory and Applications, Vol 4, 1983, pp. 109-136.

[25]Garrett, L.B., "Interactive Design and Analysis of Future Large Spacecraft Concepts," NASA Technical Paper 1937, Dec. 1981.

[26]Farmer, Jeffery T., D.M. Wahls, R.L. Wright, "Thermal- distortion Analysis of an Antenna Strongback for Geostationary High Frequency Microwave Applications," NASA TP 3016, 1990.

[27]Meyer, R.X., "Precision of Mesh-Type Reflectors for Large Space-Borne Antennas," 23rd Structures, Structural Dynamics and Materials Conference, Part 1, AIAA CP 823, 1982, pp. 60-65.

Reproduced with permission of the copyright owner. Further reproduction prohibited without permission.

[28]Fichter, W.B., "Reduction in RMS Error in Shallow Faceted Large Space Antennas," 24rd Structures, Structural Dynamics and Materials Conference, Part 1, AIAA CP 831, 1983, pp. 714-721.

[29]Wallace, J.M. and P.V. Hobbs, "Atmospheric Science," Academic Press, New York, NY, 1977.

[30]Cunningham, F.G., "Power Input to a Small Flat Plate from a Diffusely Radiating Sphere, with Application to Earth Satellites," NASA Technical Note D-710, August, 1961.

[31]Mahaney, J. & K.B. Strode, "Fundamental Studies of Thermal-Structural Effects on Orbiting Trusses," 23rd Structures, Structural Dynamics and Materials Conference, Part 1, AIAA CP 823, 1982, pp. 49-59.

[32]Balanis, C.A., "Antenna Theory, Analysis and Design," Harper & Row, Publishers, New York, NY, 1982.

[33]Harrison, E.F., D.R. Brooks, P. Minnis, B.A. Wielicki, W.F.Staylor, G.G. Gibson, D.F. Young, and F.M.Denn, "Diurnal Variability of Radiative Parameters Derived from ERBS and NOAA-9 Satellite Data," Proceeding of the International Radiation Symposium, Lille, France, August 1988, pp. 214-216.

[34]Parlett, B.N., "The Symmetric Eigenvalue Problem," Prentice-Hall, 1980, Englewood Cliffs, N.J.

[35]Galindo-Israel, V. & R. Mittra, "A New Series Representation for the Radiation Integral with Application to Reflector Antennas," IEEE Tran. on Antennas and Progagation, Vol. AP-25, No. 5, Sept. 1977, pp. 631-641.

[36]Mittra, R., Y. Rahmat-Samii, V. Galindo-Israel, & R. Norman, "An Efficient Technique for the Computation of Vector Secondary Patterns of Offset Paraboloid Reflectors," IEEE Trans. on Antennas and Propagation, Vol. AP-27, No. 3, May 1979, pp. 294-304.

[37]Bhatia, A.B., & E. Wolf, "On the Circle Polynomials of Zernike and Related Orthogonal Sets," Proc. Camb. Phil. Soc., Vol 50, 1954, pp. 40-48.

[38]Abramowitz, M., & I.A. Stegun, "Handbook of Mathematical Functions," Dover Publications, Inc., New York, NY, 1965.

[39]Noll, R.J., "Zernike polynomials and atmospheric turbulence," J. Opt. Soc. Am., Vol. 66, No. 3, March 1976.

Reproduced with permission of the copyright owner. Further reproduction prohibited without permission.

Appendix A - Zernike Polynomials

Zernike polynomials have been used extensively in optics for describing the aberration function for circular apertures and for representing the classical aberrations, for example, piston, tilt, coma, astigmatism, etc. They have found limited use in the radio frequency literature, perhaps because their principal application is to circular apertures with uniform illumination, which is not always the case for antennas. They are used under the name of 'modified Jacobi polynomials' for representing the far field when the feed is offset from the focus[35] and for calculating secondary patterns for offset reflectors.[36] Though these applications were not the motivation for the current approach, there are similiarities. The main motivation is that Zernike polynomials provide a convenient set of functions to represent wave front phase as demonstrated by their extensive use in optics[14] and because they are orthogonal and complete over the unit circle[37] with respect to the ring of real polynomials in x and y. This section provides the definition of the Zernike polynomials, some properties of interest for their application to Rf performance calculations, and new recursion relations that are use for numerical calculations.

In real form the Zernike polynomials are defined as

$\Phi_{nm}(\rho,\theta) = R_{nm}(\rho)\cos m\theta$ and $\Psi_{nm}(\rho,\theta) = R_{nm}(\rho)\sin m\theta$,

with $n = 0, 1, 2,...$ and $m \in M_n$ where $M_n = \{m \mid 0 \le m \le n$ and $n-m$ is even $\}$ and where $0 \le \rho \le 1$ is the normalized radial distance and θ is the angular coordinate, i.e. ρ and θ are the usual polar coordinates for the unit circle. It will be seen that Φ_{nm} and Ψ_{nm} are each polynomials in $x = \rho\cos\theta$ and $y = \rho\sin\theta$. The radial polynomials R_{nm} can be related to

Reproduced with permission of the copyright owner. Further reproduction prohibited without permission.

the Jacobi polynomials, can be derived from a generating function or can be obtained from the series[14]:

$$R_{nm}(\rho) = \sum_{s=0}^{(n-m)/2} (-1)^s \frac{(n-s)!}{s!\,[(n+m)/2 - s]!\,[(n-m)/2 - s]!} \rho^{n-2s}.$$

The radial polynomial R_{nm} is a polynomial of degree n with a minimum exponent of m. A few of the radial polynomials are shown in table B-1 and plotted in figure B-1.

Series Expansion of Functions

Any function $f(\rho, \theta)$ that has a Taylor series expansion about the origin and radius of convergence at least one can be expanded in terms of the Zernike polynomials over the unit circle, that is

$$f(\rho, \theta) = \sum_{n=0}^{\infty} \sum_{m \varepsilon M_n} A_{nm}\, \Phi_{nm}(\rho, \theta) + B_{nm}\, \Psi_{nm}(\rho, \theta)$$

where A_{nm} and B_{nm} are constants given by

$$\begin{Bmatrix} A_{nm} \\ B_{nm} \end{Bmatrix} = \frac{2(n+1)}{\pi(1+\delta_0^m)} \int_0^{2\pi} \int_0^1 f(\rho, \theta) \begin{Bmatrix} \Phi_{nm}(\rho, \theta) \\ \Psi_{nm}(\rho, \theta) \end{Bmatrix} \rho\, d\rho\, d\theta.$$

The factor of $2(n+1)$ comes from (Born, 1987)

$$\int_0^1 R_{nm}(\rho)\, R_{pm}(\rho)\, \rho\, d\rho = \frac{\delta_n^p}{2(n+1)}.$$

There is also the amplitude-phase version of the expansion

Reproduced with permission of the copyright owner. Further reproduction prohibited without permission.

$$f(\rho, \theta) = \sum_{n=0}^{\infty} \sum_{m \in M_n} C_{nm} R_{nm}(\rho) \cos m(\theta - \tau_{nm}).$$

where as usual $(C_{nm})^2 = (A_{nm})^2 + (B_{nm})^2$ and $\tan m\tau_{nm} = -\frac{B_{nm}}{A_{nm}}$.

Recursion Relations

The following recursion relations were developed to improve the computational efficiency of calculating values of the polynomials:

$R_{00} = 1$ to initialize the process.

$R_{n+1,n+1} = \rho R_{nn}$ for diagonal stepping with n = m,

$(n+1) R_{2n+2,0} = (2\rho^2 - 1)(2n+1) R_{2n,0} - n R_{2n-2,0}$ for generating the terms with m = 0,

$R_{n+1,m+1} = \rho (R_{nm} + R_{n,m+2}) - R_{n-1,m+1}$ for diagonal stepping starting at an m = 0 term. These can all be verified using the series expansion above. The recursion with m = 0 was derived from a recursion formula[38] for Legendre polynomials and the relation[14]

$R_{2n,0}(\rho) = P_n(2\rho^2 - 1)$

where P_n is the Legendre polynomial.

Using simple trigonometry identities leads to the corresponding recursion relations for the Zernike polynomials Φ_{nm} and Ψ_{nm}:

$\Phi_{00} = 1$ and $\Psi_{00} = 0$ for initialization,

$\Phi_{n+1,n+1} = x \Phi_{nn} - y \Psi_{nn}$ and $\Psi_{n+1,n+1} = y \Phi_{nn} + x \Psi_{nn}$

Reproduced with permission of the copyright owner. Further reproduction prohibited without permission.

for diagonal stepping with n = m,

$$(n+1)\,\Phi_{2n+2,0} = (2\rho^2-1)(2n+1)\,\Phi_{2n,0} - n\,\Phi_{2n-2,0}$$

for the terms with m = 0, which can be seen to be even polynomials in ρ and thus even and symmetric polynomials in x and y as expected,

$$\Phi_{n+1,m+1} = x\,(\,\Phi_{nm} + \Phi_{n,m+2}\,) - y\,(\,\Psi_{nm} - \Psi_{n,m+2}\,) - \Phi_{n,m+1}$$

and

$$\Psi_{n+1,m+1} = y\,(\,\Phi_{nm} - \Phi_{n,m+2}\,) - x\,(\,\Psi_{nm} + \Psi_{n,m+2}\,) - \Phi_{n,m+1}$$

for diagonal stepping from each m = 0 term. These later relations clearly illustrate that each Zernike polynomial is in fact a polynomial in x and y.

If the antenna surface distortions is represented in terms of Zernike polynomials then the gradient of the polynomials is required for RF performance calculations, and recursive relations for these can be derived starting with the recursion relation:[39]

$$\frac{d}{d\rho} R_{nm} = n\,[\,R_{n-1,m-1} + R_{n-1,m+1}\,] + \frac{d}{d\rho} R_{n-2,m}.$$

For convience, the notation $\frac{\partial f}{\partial x} = f;_x$ will be used in the following.

In the recursion relation for the derivative, the term in brackets can be replaced using the diagonal stepping equation for $R_{n+1,\,m+1}$ to yield

$$R_{nm};\rho = n\,(R_{nm} + R_{n-2,m}) + R_{n-2,m};\rho.$$

Reproduced with permission of the copyright owner. Further reproduction prohibited without permission.

The gradients with respect to x and y are required and these can be obtain in the following manner:

$$\Phi_{nm};x = \Phi_{nm};\rho\ \rho;x + \Phi_{nm};\theta\ \theta;x.$$

Substituting the definition for Φ_{nm} and using $\rho^2 = x^2 + y^2$ and $\tan\theta = y/x$ yields:

$$\Phi_{nm};x = \frac{x\cos m\theta}{\rho^2} R_{nm},\rho + \frac{m\,y}{\rho^2}\Psi_{nm}.$$

Substituting for $R_{nm};\rho$ from above gives

$$\Phi_{nm};x = \frac{x\cos m\theta}{\rho^2}\left[\, n\,(R_{nm} + R_{n-2,m}) + R_{n-2,m};\rho\,\right] + \frac{m\,y}{\rho^2}\Psi_{nm}$$

Finally, eliminate $R_{n-2,m};\rho$ by using the expression above for $\Phi_{nm};x$ evaluated for $n = n-2$ to get

$$\Phi_{nm};x = \Phi_{n-2,m};x + \frac{n\,x}{\rho^2}(\Phi_{nm} + \Phi_{n-2,m}) + \frac{m\,y}{\rho^2}(\Psi_{nm} - \Psi_{n-2,m}).$$

A similiar development gives the other three recursions:

$$\Phi_{nm};y = \Phi_{n-2,m};y + \frac{n\,y}{\rho^2}(\Phi_{nm} + \Phi_{n-2,m}) - \frac{m\,x}{\rho^2}(\Psi_{nm} - \Psi_{n-2,m}).$$

$$\Psi_{nm};x = \Psi_{n-2,m};x + \frac{n\,x}{\rho^2}(\Psi_{nm} + \Psi_{n-2,m}) - \frac{m\,y}{\rho^2}(\Phi_{nm} - \Phi_{n-2,m}).$$

$$\Psi_{nm};y = \Psi_{n-2,m};y + \frac{n\,y}{\rho^2}(\Psi_{nm} + \Psi_{n-2,m}) + \frac{m\,x}{\rho^2}(\Phi_{nm} - \Phi_{n-2,m}).$$

Reproduced with permission of the copyright owner. Further reproduction prohibited without permission.

These recursions increment n for a fixed m and are started at n = m. The starting conditions are easily derived from $\Phi_{nn} = \rho^n \cos n\theta$, etc. Differentiation as above gives

$$\Phi_{nn;x} = \frac{n}{\rho}(x\,\Phi_{nn} + y\,\Psi_{nn}), \qquad \Phi_{nn;y} = \frac{n}{\rho}(y\,\Phi_{nn} - x\,\Psi_{nn}),$$

$$\Psi_{nn;x} = \frac{n}{\rho}(x\,\Psi_{nn} - y\,\Phi_{nn}), \qquad \Psi_{nn;y} = \frac{n}{\rho}(y\,\Psi_{nn} + x\,\Phi_{nn}).$$

The gradient recursions are not defined at $\rho = 0$; but, all gradients are zero except when m = 1, then it is easily shown that

$$\Phi_{n,1;x} = \Psi_{n,1;y} = (-1)^{n+1}\, n \text{ and } \Phi_{n,1;y} = \Psi_{n,1;x} = 0 \text{ for } \rho = 0.$$

Normalization

The polynomials above are normalized so that the maximum absolute value of each polynomial is one on the circle $\rho = 1$. It is some times convient to normalize the polynomials so that each polynomial has a RMS value of unity over the unit circle, i.e.

$$\frac{1}{\pi}\int_0^1 \int_0^{2\pi} \Phi_{nm}\,\Phi_{pm}\,\rho\,d\rho\,d\theta = \delta_n^p$$

and similarily for Ψ_{nm}. To implement this normalization each polynomial above must be multiplited by a normalization constant a_n where $a_n = \sqrt{2(n+1)}$ if $m \neq 0$ and $a_n = \sqrt{n+1}$ if $m = 0$.[39]

Reproduced with permission of the copyright owner. Further reproduction prohibited without permission.

m\n	0	1	2	3	4	5
0	1		$2\rho^2-1$		$6\rho^4-6\rho^2+1$	
1		ρ		$3\rho^3-2\rho$		$10\rho^5-12\rho^3+3\rho$
2			ρ^2		$4\rho^4-3\rho^2$	
3				ρ^3		$5\rho^5-4\rho^3$
4					ρ^4	
5						ρ^5

Table A-1. Zernike radial polynomials, $R_{nm}(\rho)$.

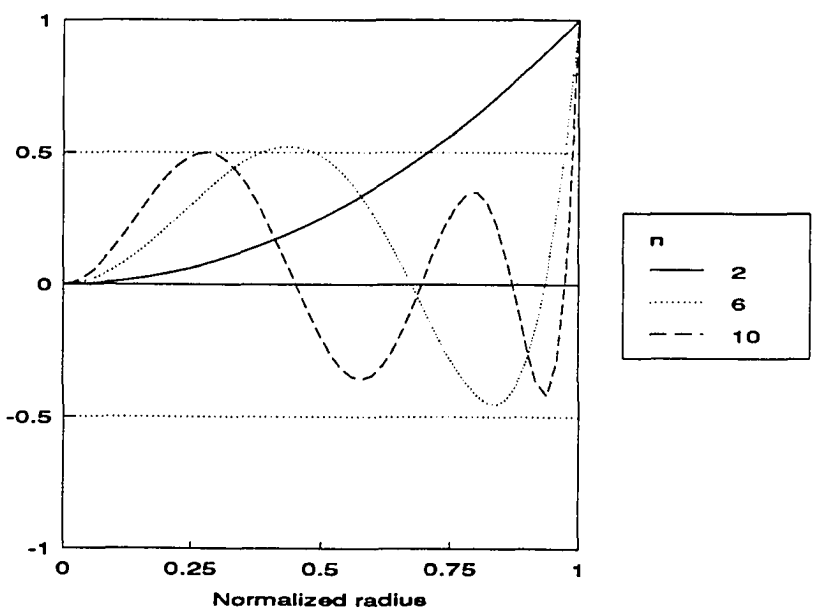

Figure A-1. Variation of selected radial polynomials, R_{n2}.

Reproduced with permission of the copyright owner. Further reproduction prohibited without permission.

Appendix B - 55m Radiometer Geometry

This appendix contains the NASTRAN graphical output showing the grid points and rods that form the structure of the 55m tetrahedral truss.

Reproduced with permission of the copyright owner. Further reproduction prohibited without permission.

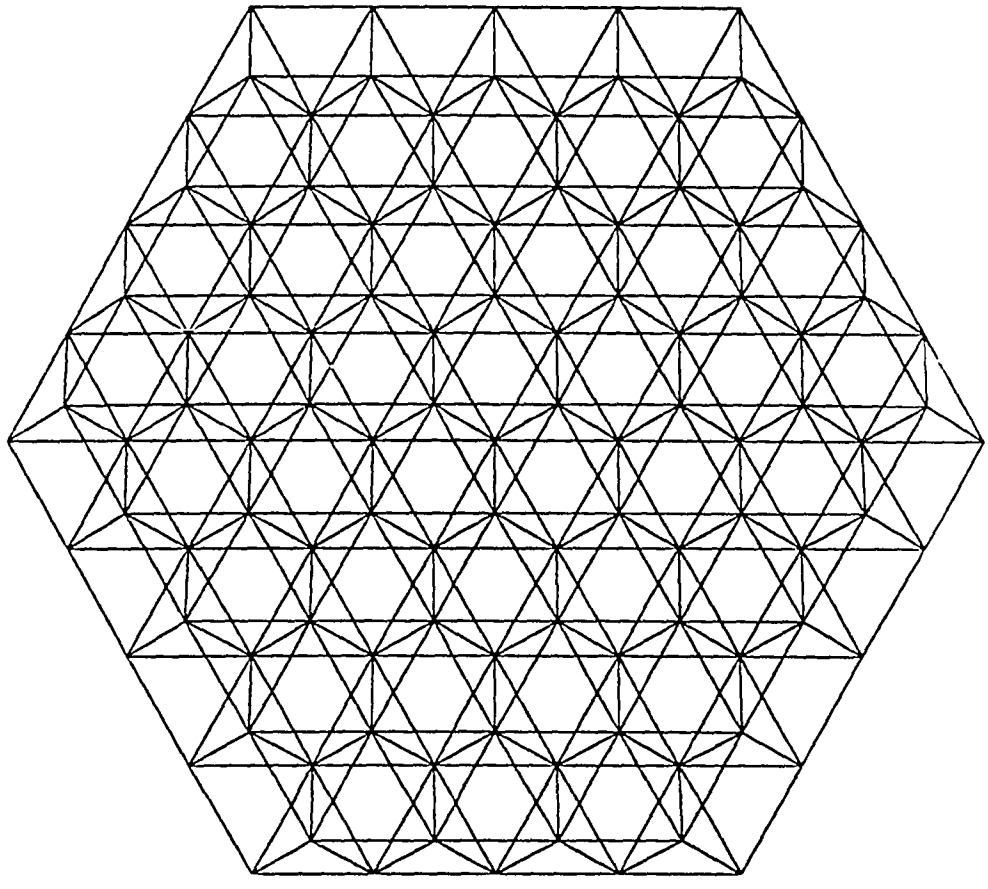

Figure B-1. View of antenna along the z axis showing 420 rods.

Reproduced with permission of the copyright owner. Further reproduction prohibited without permission.

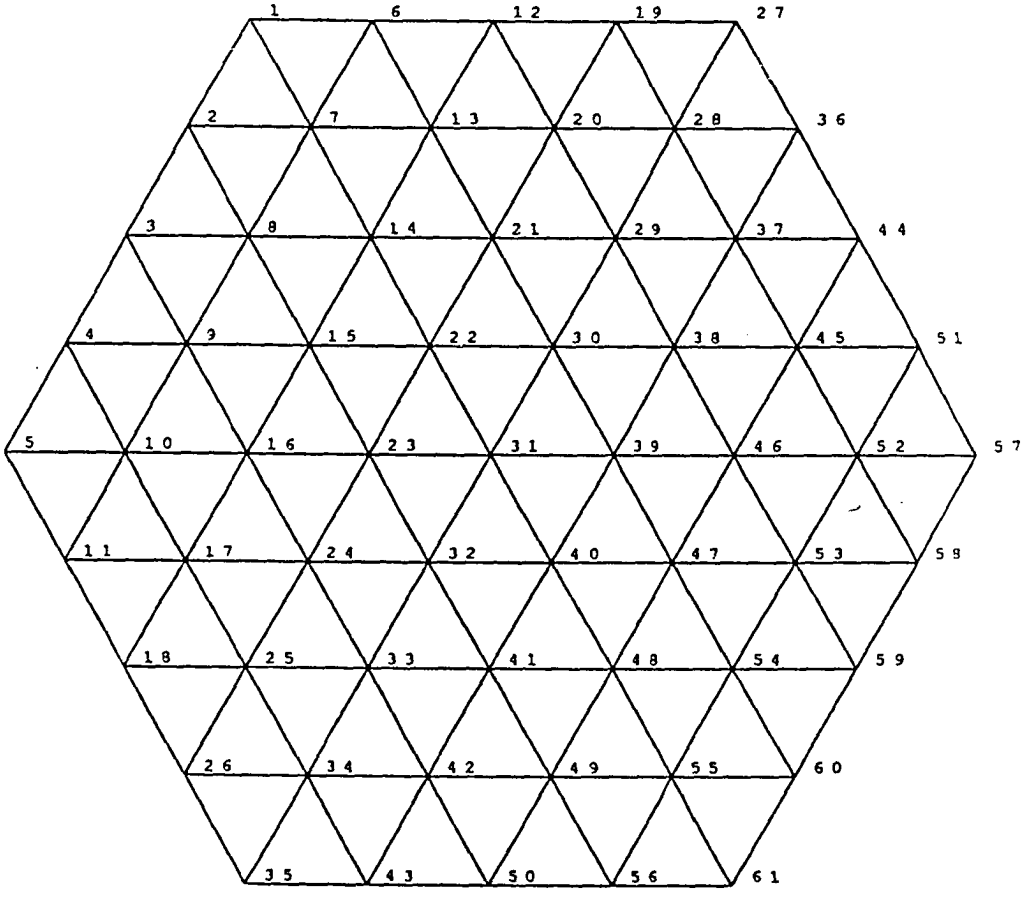

Figure B-2. View of the 156 front surface rods with grid points numbered.

Reproduced with permission of the copyright owner. Further reproduction prohibited without permission.

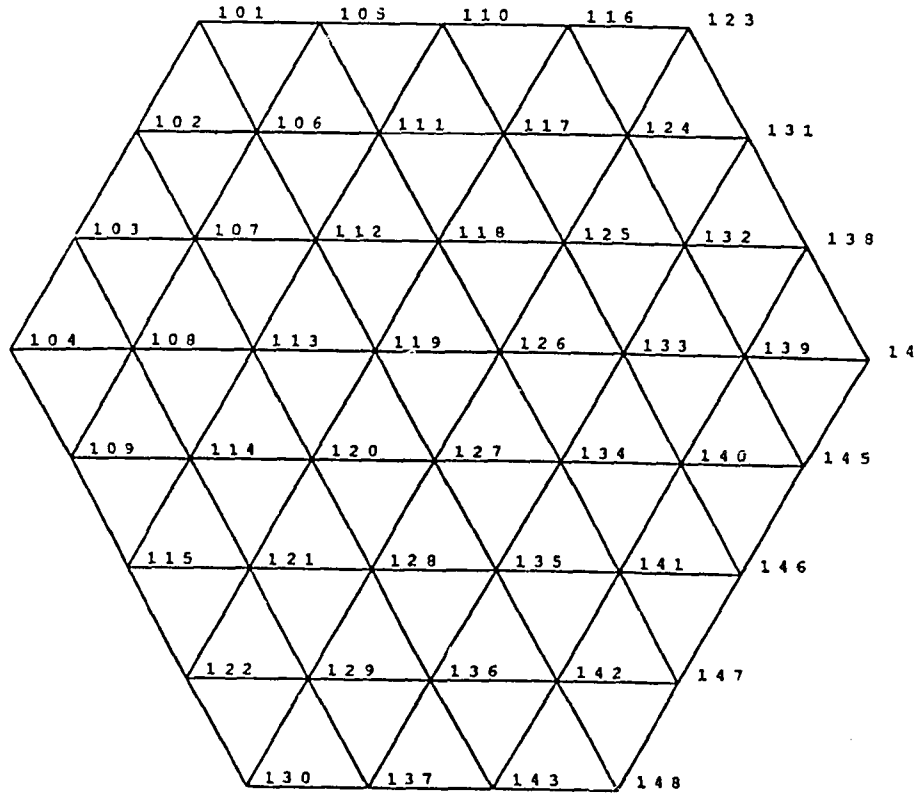

Figure B-3. View of the 120 back surface rods with grid points numbered.

Reproduced with permission of the copyright owner. Further reproduction prohibited without permission.

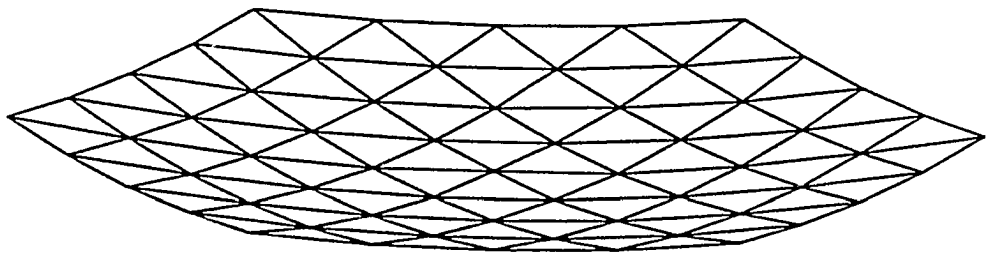

Figure B-4. View of front surface rods from 15^{o} elevation.

Reproduced with permission of the copyright owner. Further reproduction prohibited without permission.